© 2017. Published by The Company of Biologists Ltd | Development (2017) 144, 4462-4472 doi:10.1242/dev.150557

TECHNIQUES AND RESOURCES

RESEARCH ARTICLE

Multi-scale quantification of tissue behavior during amniote embryo axis elongation

Bertrand Bénazéraf[1,2,*,‡], Mathias Beaupeux[3], Martin Tchernookov[3], Allison Wallingford[2], Tasha Salisbury[2], Amelia Shirtz[2], Andrew Shirtz[4], David Huss[2,5], Olivier Pourquié[1,6,7,8,‡], Paul François[3,‡] and Rusty Lansford[2,9,‡]

ABSTRACT

Embryonic axis elongation is a complex multi-tissue morphogenetic process responsible for the formation of the posterior part of the amniote body. How movements and growth are coordinated between the different posterior tissues (e.g. neural tube, axial and paraxial mesoderm, lateral plate, ectoderm, endoderm) to drive axis morphogenesis remain largely unknown. Here, we use quail embryos to quantify cell behavior and tissue movements during elongation. We quantify the tissue-specific contribution to axis elongation using 3D volumetric techniques, then quantify tissue-specific parameters such as cell density and proliferation. To study cell behavior at a multi-tissue scale, we used high-resolution 4D imaging of transgenic quail embryos expressing fluorescent proteins. We developed specific tracking and image analysis techniques to analyze cell motion and compute tissue deformations in 4D. This analysis reveals extensive sliding between tissues during axis extension. Further quantification of tissue tectonics showed patterns of rotations, contractions and expansions, which are consistent with the multi-tissue behavior observed previously. Our approach defines a quantitative and multi-scale method to analyze the coordination between tissue behaviors during early vertebrate embryo morphogenetic events.

KEY WORDS: Confocal microscopy, Live imaging, Quail embryo, Axis elongation, Proliferation, PSM, Multi-tissue, Tissue deformations, Morphogenesis

INTRODUCTION

Axis formation in the vertebrate embryo occurs in a head-to-tail sequence; the anterior part of the body starts to form first followed by the thoracic and later on the lumbosacral regions. During this series of events, the different embryonic layers (endoderm, mesoderm and ectoderm) extend towards the posterior pole of the embryo while they progressively organize into more differentiated tissue structures anteriorly. As these structures emerge, they display a stereotypical multi-tissue 3D organization: the neural tube is flanked by two strips of presomitic paraxial mesoderm (PSM) laterally, by the notochord and endoderm ventrally, and by the ectoderm dorsally.

Technological advances in microscopy have significantly improved our understanding of the morphogenetic events that control vertebrate axis formation, in particular by allowing observation of cellular behaviors over different stages of development. Pioneer studies using frog and fish embryos indicate that convergent extension is a central mechanism for the formation of the anterior part of the body axis of vertebrates (Shih and Keller, 1992a,b; Warga and Kimmel, 1990). During convergent extension, cells migrate and intercalate, which causes the narrowing of the tissues in one direction and their elongation in the perpendicular direction. This process is conserved in amniotes as it has been documented in chicken (Lawson and Schoenwolf, 2001) and mouse (Ybot-Gonzalez et al., 2007). In the second phase of elongation, which follows this first phase of large convergent extension movements, the axis extends without considerable change in its width. During this phase, the growth of the caudal region of the embryo is thought to be crucial to the elongation process. By deleting caudal structures and developing time-lapse imaging analysis to identify the regions controlling axis elongation in the avian embryo, we previously highlighted the crucial role of paraxial mesoderm in axis extension and provided evidence of the graded random motility of cells as a primary driver of elongation (Bénazéraf et al., 2010). Although this newly described collective behavior was demonstrated to be important in posterior tissue elongation, it does not explain how movements and growth are coordinated between different tissues in the posterior part of the elongating embryo.

The recent development of tools for analyzing the movements of vast numbers of cells has allowed for better understanding of the complexity of axis morphogenesis. Analyzing cell movements within the tail bud of zebrafish embryos revealed that coherence in collective migration and tissue flow is essential for elongation (Lawton et al., 2013). Interfering with cell/fibronectin interactions disturbed multi-tissue mechanics in this process (Dray et al., 2013). These data suggest that large-scale collective migration processes and multi-tissue mechanics are a crucial part of the elongation process in fish embryos. We recently established transgenic quails that allow for the study of global 3D multi-tissue kinetics in real time in amniote embryos (Huss et al., 2015). These transgenic quails (referred to as the H2B-Cherry line) ubiquitously express a nuclear fluorescent protein (H2B-Cherry), which allows for the

[1]Department of Development and Stem cells, Institut de Génétique et de Biologie Moléculaire et Cellulaire (IGBMC), CNRS (UMR 7104), Inserm U964, Université de Strasbourg, 67400 Illkirch Graffenstaden, France. [2]Department of Radiology and Developmental Neuroscience Program, Saban Research Institute, Children's Hospital Los Angeles, Los Angeles, CA 90027, USA. [3]Department of Physics, Ernest Rutherford Physics Building, McGill University, 3600 rue University, Montréal, QC, H3A 2T8, Canada. [4]Northern Michigan University, Computer Science and Mathematics Department, Marquette, MI 49855, USA. [5]Department of Biological Sciences, University of Southern California, Los Angeles, CA 90089, USA. [6]Department of Pathology, Brigham and Women's Hospital, 60 Fenwood Road, Boston, MA 02115, USA. [7]Department of Genetics, Harvard Medical School, 60 Fenwood Road, Boston, MA 02115, USA. [8]Harvard Stem Cell Institute, 60 Fenwood Road, Boston, MA 02115, USA. [9]Department of Radiology and Development, Stem Cells, and Regenerative Medicine (DSR), Keck School of Medicine, University of Southern California, Los Angeles, CA 90033, USA.
*Present address: Centre de Biologie du Développement (CBD), Centre de Biologie Intégrative (CBI), Université de Toulouse, CNRS, UPS, France.

‡Authors for correspondence (bertrand.benazeraf@univ-tlse3.fr; pourquie@genetics.med.harvard.edu; paulf@physics.mcgill.ca; rustylansford@gmail.com)

T.S., 0000-0001-6012-0264; A.S., 0000-0001-5628-395X; D.H., 0000-0002-3239-8477; R.L., 0000-0002-2159-3699

Received 15 February 2017; Accepted 10 August 2017

Development (2017) 144, 4462-4472 doi:10.1242/dev.150557

visualization of every nucleus in every tissue of the embryo. Specific algorithms and computational methods have been designed to analyze global tissue deformations in embryos (Blanchard et al., 2009; Rauzi et al., 2015; Rozbicki et al., 2015). However, this type of analysis has not been achieved at the multi-tissue scale in the context of axis elongation of higher vertebrate embryos.

In this work, we aimed to understand the coordination of growth and movements in the different tissues composing the posterior region of the embryo that allows posterior elongation and organization of the future organs. We used two-photon laser imaging on fixed quail embryos to thoroughly assess tissue-specific behaviors regarding volume change, cell proliferation, and apoptosis at different stages of axis extension. To analyze elongation at the whole structure level dynamically, we used time-lapse imaging of H2B-Cherry transgenic quail embryos to track cell movements and numerically compute related tissue deformations. Our analysis reveals emergent coordinated motions of multiple tissues, with graded strain rates and highly rotational flows in paraxial mesoderm. Altogether we display a new method to analyze the coordination between tissue-specific cell behaviors and tissue kinetics during axis elongation.

RESULTS

Volume gain varies among tissues during axis extension

As an embryo elongates, the volumes of its different tissues are changing. The relative participation of each tissue in the overall embryonic volume increase is currently unknown. To identify tissue volume changes during axis elongation, we imaged, cleared, and DAPI-stained embryos at different stages of development [11s (11 pairs of somites), 13s and 15s] by two-photon microscopy. We then analyzed these images by reconstructing the 3D structures of the posterior part of the embryo and manually delineated the different tissue volumes based on morphological clues: neural tube, notochord, paraxial mesoderm, progenitor region (the axial region located caudally to the notochord containing the neuro-mesodermal progenitors) (Fig. 1A). For all tissues, we used the boundary between somite 9 and 10 as an anterior reference because it represents a fixed position readily discernable between embryos. We observed an overall volume increase of the posterior part of the embryo (Fig. 1B). Interestingly, distinct posterior tissues gained volume at different rates (Fig. 1C). For example, the paraxial mesoderm, which constitutes a significant part of the whole tissue volume, grows at an average rate of 3.3×10^6 μm^3/h whereas the neural tube expands at a rate of 1×10^6 μm^3/h (n=3 embryos for each condition). However, notochord and the axial progenitor zone do not gain significant volume over time.

To determine whether the observed tissue volume variations are anisotropic or isotropic, we measured whether changes are due to gain in length, width or thickness. The analysis shows that the volume expansion is mainly due to an increase in length (Fig. 1D), confirming the high anisotropy due to the anteroposterior extension at the tissue level.

To improve our volume measurements, we used tissue-specific marker expression to delimit areas with low morphological cues; for example, the boundary between the lateral plate and PSM or between the tip of the notochord and progenitor zone. We performed immunostaining with the pan-neural marker Sox2 and pan-mesodermal marker Brachyury to measure specifically the volumes of the neural tube, the notochord, the caudal PSM and the progenitor zone. This analysis confirmed our previous results by showing that the paraxial mesoderm and the neural tube have the fastest volume expansion rate (Fig. S1). Altogether, these results show that growth rates between tissues differ tremendously and individual tissues mostly expand in the anteroposterior direction during axis extension.

Cell density patterns and cell size are tissue specific and conserved across stages

Tissue volume changes can be due to a gain in cell number, or a difference in spacing between cells (Li et al., 2015). To discriminate between these possibilities, we calculated the cell density of the posterior part of elongating embryos. Segmentation algorithms (see Materials and Methods) were used to localize every nucleus of DAPI-stained and 3D-reconstructed embryo images. Densities were computed by calculating the distances between ten neighbor nuclei. The different distances were averaged to obtain a tissue density map (number of cells/100 μm^3) at various stages of development (Fig. 2A-C). Interestingly, we observed a pattern of regionally conserved densities at different embryonic stages. For example, the neural tube and lateral plate have higher densities than caudal PSM, endoderm and ectoderm. To quantify and compare the tissue-specific cell densities we calculated the average density of tissue across all three stages. The results showed that average densities were different between tissues. For instance, the neural tube, notochord and lateral plate had average densities higher than the paraxial mesoderm, the progenitor zone or the endoderm (Fig. 2D, Fig. S2). However, when comparing different stages of development, most of the average tissue densities are not significantly different (Fig. 2E, Fig. S2). In addition to the inter-tissue density differences across stages, our analysis also revealed intra-tissue density differences. For instance, we measured a caudo-rostral gradient of increasing cell density in the PSM at the three different time points (Fig. 2A-C, purple arrowheads). Altogether, these results show that cell densities vary within and among tissue types and that these differences are conserved during axis extension. As our measure of cell densities was based on the measurement of the distance between nuclei, we wanted to know whether those differences could reflect cell size difference between tissues. To test this possibility, we estimated the cell size by measuring the long and short axis of representative cells in the different tissues at different stages (Fig. S3A) (see supplementary Materials and Methods). Here again, this series of measurements showed a distinct distribution of cell size between tissues (Fig. S3B). For instance, endodermal and ectodermal cells were bigger whereas the notochord and neural tube contained smaller cells. These differences were conserved at the different stages of elongation (Fig. S3C). As for the cell density, cell size analysis showed tissue-specific differences that were conserved through the elongation process. Altogether, these data strongly suggest that tissue expansion during elongation is not due to cell density or cell size changes and could therefore mostly be due to cell number changes.

Proliferation and apoptosis show tissue-specific patterns during elongation

To test whether tissue-specific cell proliferation could be responsible for the different tissue volume growth rates, we used cumulative 5-ethynyl-2'-deoxyuridine (EdU) staining to determine cell cycle length (Warren et al., 2009; Nowakowski et al., 1989). We treated embryos with EdU for 3 h, 6 h or 9 h and saw a gradual increase in incorporation of EdU in cells of the posterior part of the embryo (Fig. 3A-C). We then determined the rate of incorporation for each tissue and treatment (Fig. 3D,D′) which allowed us to calculate the cell cycle times for each tissue (see supplementary

Development (2017) 144, 4462-4472 doi:10.1242/dev.150557

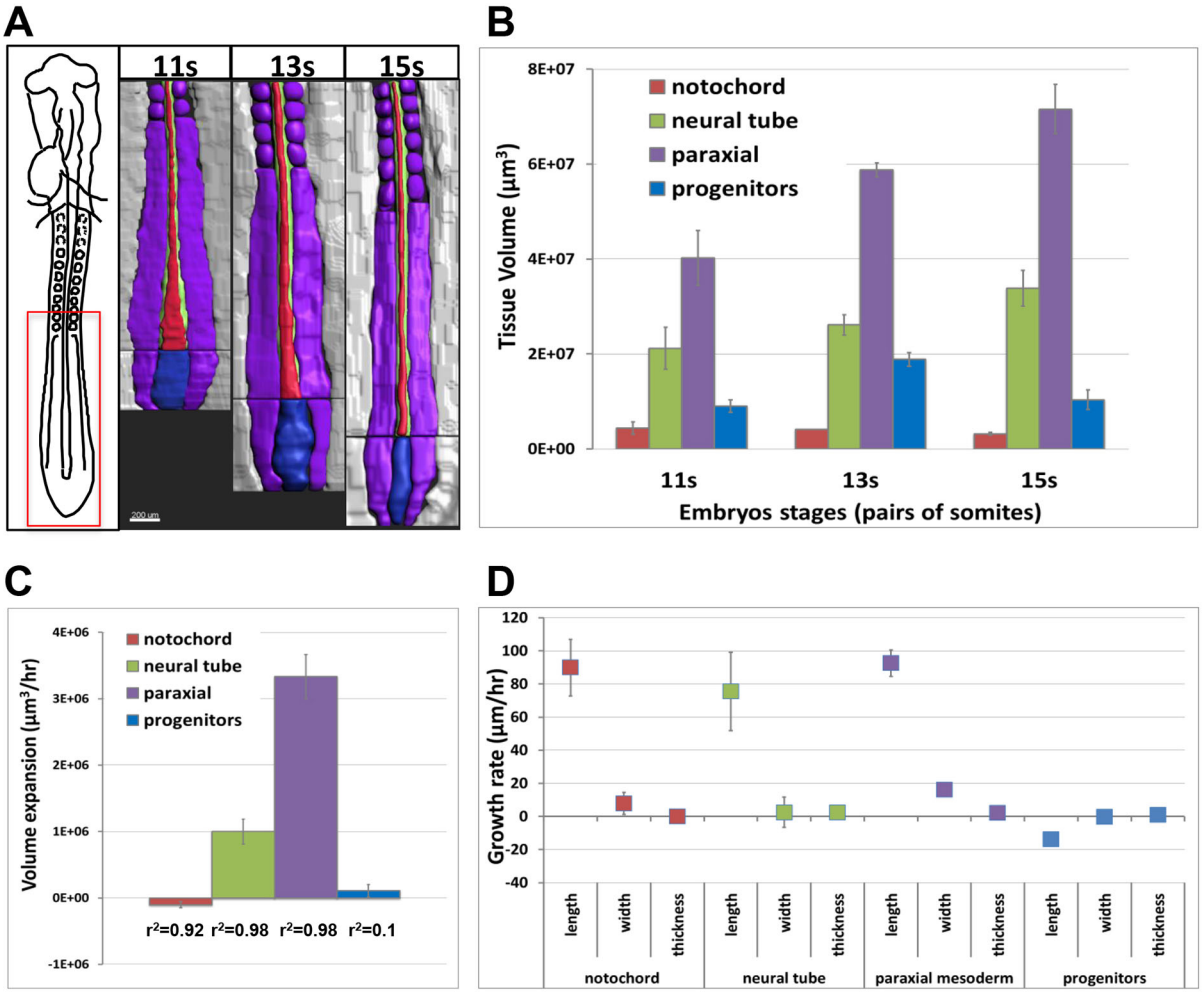

Fig. 1. Tissue volume growth during axis extension. (A) 3D representation/drawing of different tissues forming the posterior part of quail embryo during axis extension (area of interest is shown in the red rectangle of the scheme on the left, ventral view; anterior side is at the top). The samples are a representative 11 pairs of somites embryo (left), a 13 pairs of somites embryo (middle) and a 15 pairs of somites embryo (right). The progenitor zone is in blue, the paraxial mesoderm is in purple, the notochord is in red, and the neural tube is in green. (B) Tissue volume measurements for the different stages of development [n=3 embryos per stage (total nine embryos)]. (C) The rate of tissue volume expansion for the various tissues over time (µm^3/h). r^2 is calculated for the linear regression of the slope of volume variations. (D) The rate of tissue expansion for the different tissues in the three dimensions (x,y,z) over time (µm/h). Error bars represent s.e.m.

Materials and Methods and Nowakowski et al., 1989). Remarkably, we saw that cell cycle times vary from 8 to 28 h (notochord ∼28 h, ectoderm ∼14 h, endoderm ∼12 h, progenitor zone ∼11.5 h, neural tube ∼11 h, lateral plate ∼10 h and paraxial mesoderm ∼9 h) (Fig. 3E). When comparing cell cycle times of different tissues with each other, we found that 11 out of 22 comparisons were significantly different (P<0.05, n=9) (Fig. S4). These results show that in the developing posterior embryo tissues are proliferating at different rates: notochord cells cycle the slowest, endoderm and ectoderm cycle at an intermediate cell cycle time, and cells in paraxial mesoderm, lateral mesoderm, neural tube and the axial progenitors zone cycle faster. These results correlate well with the analysis of tissue volume changes as the two tissues that expand the fastest – the neural tube and the paraxial mesoderm – are also the tissues with the shortest cell cycle times (10 h and 8 h, respectively).

To see whether there were anteroposterior differences in cell cycle lengths, we measured the cell cycle time at the levels of the anterior PSM (rostral), the caudal PSM (caudal) and the progenitor region (very caudal). Whereas the proliferation speeds within the notochord and endoderm changed significantly along the anteroposterior (A/P) axis, the tissue cell cycle length did not differ significantly along the A/P axis within the PSM, ectoderm, neural tube or lateral plate mesoderm (Fig. S4). Altogether, our results show that during axis elongation posterior tissues have different cell cycle times.

To assess a potential role of cell death in axis elongation, we next examined the rate of apoptosis within the various posterior tissues of the elongating embryo. By combining terminal deoxynucleotidyl transferase dUTP nick end labeling (TUNEL) and DAPI staining in 11s, 13s and 15s quail embryos we were able to estimate the rate of cell death in 3D (Fig. S5). The cell death rate did not exceed 5% in any of the tissues, and cell death patterns were similar to published data in chicken embryos, suggesting that these patterns are conserved between chicken and quail embryos (Tenin et al., 2010; Olivera-Martinez et al., 2012). We observed, however, that some tissues exhibited a higher rate of cell death than others. For instance, the ectoderm had a cell death rate of 3.6% whereas the axial progenitor zone had the lowest cell death rate of 0.6%. Although cell death only concerns a small proportion of cells, our data show that cell death seems to be regulated in a tissue-specific manner.

As a whole, our data show that proliferation and cell death display tissue-specific patterns in the elongating embryo, and therefore

Development (2017) 144, 4462-4472 doi:10.1242/dev.150557

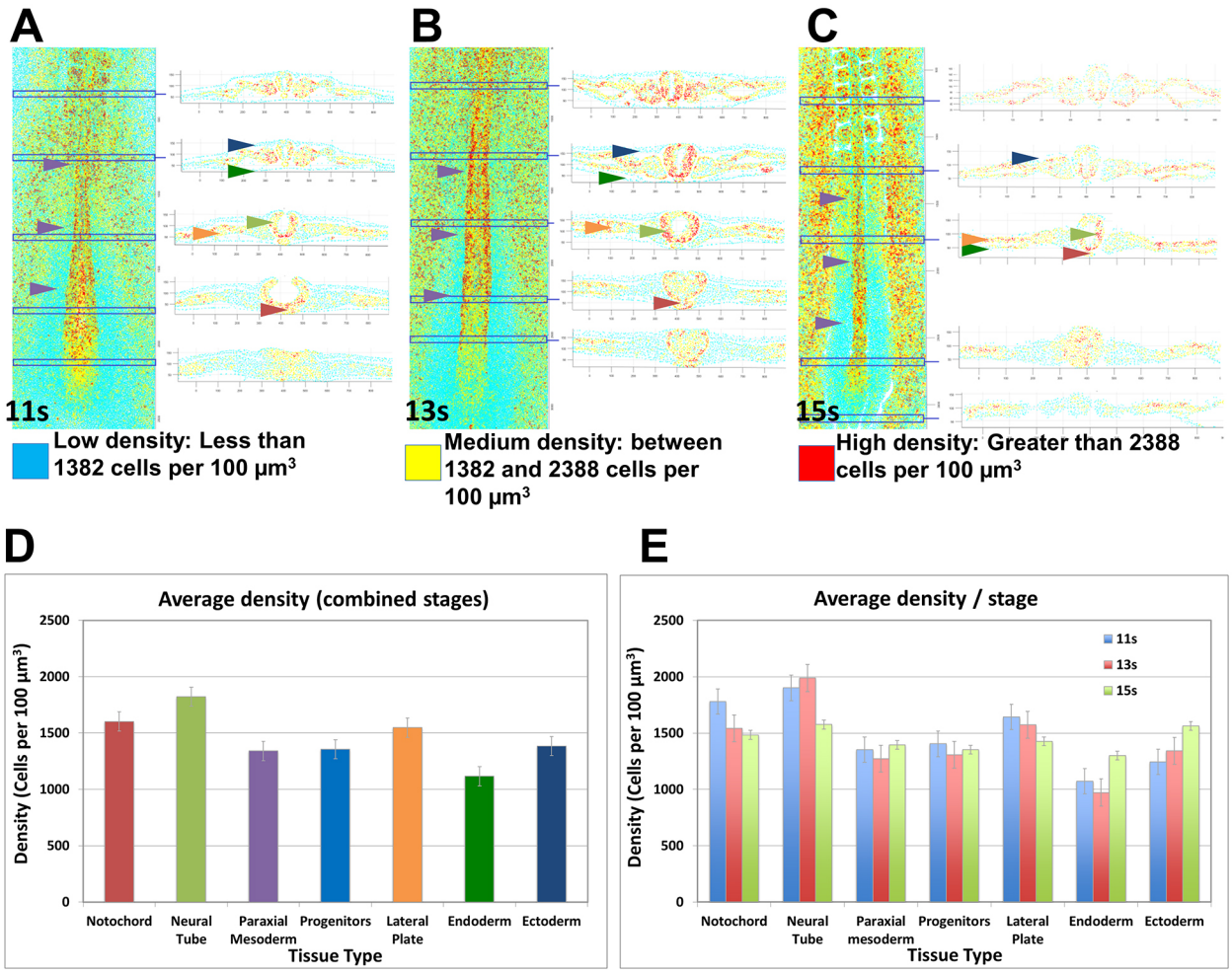

Fig. 2. Cell density in the elongating embryo. (A-C) 3D density map (dorsal view) and associated transverse sections of representative embryos at different stages. 11 pairs of somites (A), 13 pairs of somites (B), 15 pairs of somites (C). Colors represent average cell densities: cyan codes for density lower than 1382 cells/100 µm^3, yellow codes for density between 1382 and 2388 cells/µm^3, red codes for density higher than 2388 cells/µm^3. The cell densities for PSM, endoderm and ectoderm are low (purple, green, blue arrowheads, respectively), cell densities for the notochord, neural tube and lateral plate are medium to high (red, light green and orange arrowheads, respectively); note that within the paraxial mesoderm there is a caudal-to-rostral increasing gradient of cell density (purple arrowheads). (D) Average cell density by tissue across stages 11, 13 and 15 pairs of somites (total nine embryos). (E) Average cell density per stage (n=3 embryos per stage). Error bars represent s.e.m. Note that the relative pattern of tissue densities across all three stages (shown in D) is conserved during each of the individual stages analyzed (11, 13, 15 pairs of somites, E).

these mechanisms could participate in the differential volume growth related to the elongation process. For instance, PSM has a fast proliferation and a low cell death rate which might explain part of the highest volume expansion for this tissue.

Fitting tissue proliferation rates to the elongation process

After we characterized different tissue-specific cellular behaviors experimentally, we wanted to explore their potential influence on axis elongation. To determine whether the difference in proliferation and expansion could partly explain the multi-tissue kinetics, we fitted the different measured cell cycle lengths and compared them with the observed elongation. We adapted several parameters to facilitate this process. We simplified the embryo to a 2D structure composed of four different tissues (paraxial mesoderm, progenitor zone, neural tube and notochord). Because volume expansion is mostly due to growth in the anteroposterior direction (Fig. 1C), we excluded growth in the dorsoventral and mediolateral directions. We imposed an elongation rate on each tissue based on experimentally measured proliferation rates (Fig. 3E), e.g. 28 h for notochord, 11.5 h for progenitor zone, 9 h for PSM to a virtual 11s embryo (with tissue lengths based on averaged measures made at 11s) (see supplementary Materials and Methods). We then compared the tissue lengths between this 11s embryo virtually grown for 6 h and the experimental measurements made in 15s embryos (which is approximately the stage that an 11s embryo would reach in 6 h). The comparisons between this 'proliferation only' theoretical simulation and measured tissue growth are therefore indicative of the effect of proliferation in elongation. We found that simulated growth rates of paraxial mesoderm, neural tube and the progenitor region were highly similar to the measured growth (Fig. 4A). These findings indicate that proliferation could be responsible for part of the expansion of these tissues.

In contrast, the simulated length of the notochord was significantly shorter than its measured length at 15s, and therefore proliferation alone cannot explain the elongation of the notochord. It is known that cell rearrangements such as intercalation take place in the context of notochord elongation (Keller et al., 1989) and could, therefore, play a role in elongation. However, because the notochord is physically linked to the progenitor region, which moves in a

Development (2017) 144, 4462-4472 doi:10.1242/dev.150557

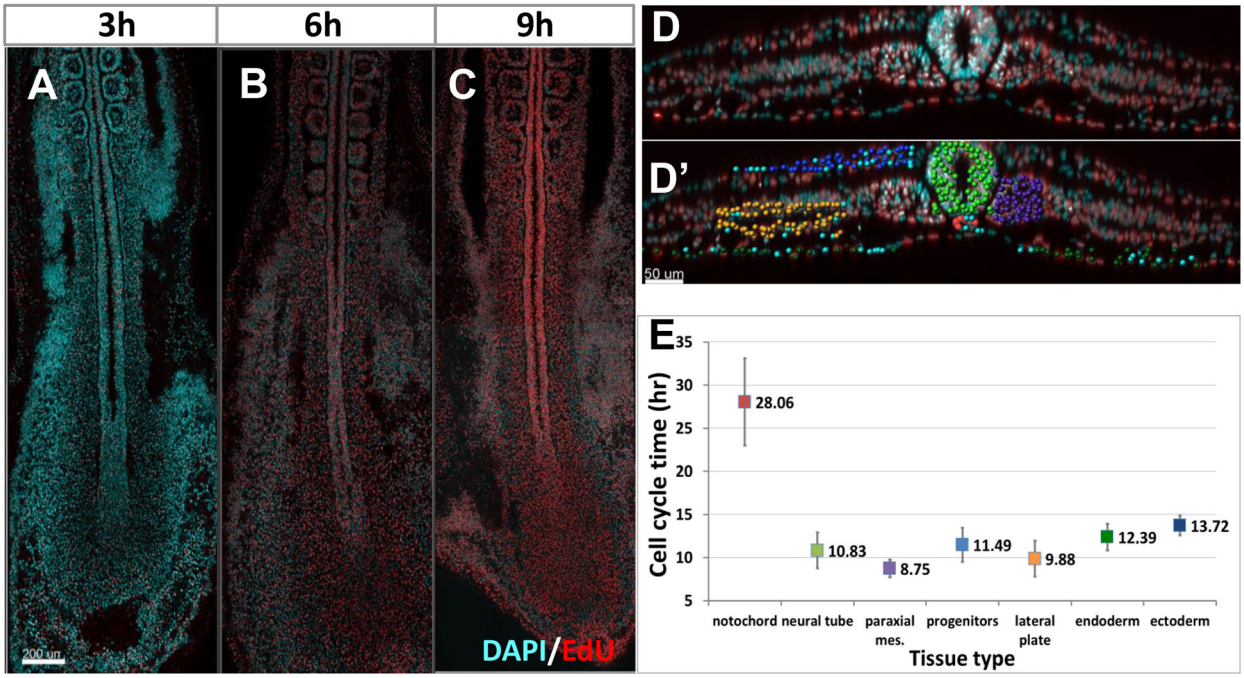

Fig. 3. Proliferation analysis during axis extension. (A-C) EdU (red) and DAPI (cyan) labeling after different EdU pulse length time on stage 11 HH quail embryo: 3 h EdU (A), 6 h (B), 9 h (C) (digital confocal coronal slices, anterior is at the top). Note that the longer the pulse, the more cells are stained with EdU. (D) An example of quantification of 6 h EdU-positive cells for the different tissues on a digital transverse section of a 3D reconstruction: red is EdU positive, cyan is DAPI. (D′) EdU-positive cells are automatically detected and color-coded depending on the tissue they belong to (paraxial mesoderm is purple, notochord is red, the neural tube is green, ectoderm is dark blue, endoderm is dark green, lateral plate is orange), EdU-negative cells are marked by a light blue spot. (E) Cell cycle time (in hours) for the different tissues calculated from the rate at which the percentage of EdU-positive cells increases as a function of pulse time. For each tissue, measurements were made in three different regions along the A/P axis, in three different embryos per EdU pulse (total nine embryos). Error bars represent s.e.m.

caudal direction, our simulation indicates that notochord tissue could slide in relation to surrounding tissues such as the paraxial mesoderm (Fig. 4B). Altogether, these simulations suggest that differential proliferation is part of a tissue-specific coordinative morphogenetic program at work in the posterior part of the developing embryo.

Embryonic tissues slide during axis elongation

The fact that tissues are growing at different rates suggests that they might elongate at different speeds. To further understand cell movements and tissue dynamics during axis elongation, we used transgenic quail embryos and time-lapse imaging. *PGK1:H2B-chFP* is a transgenic quail line in which the expression of a fusion

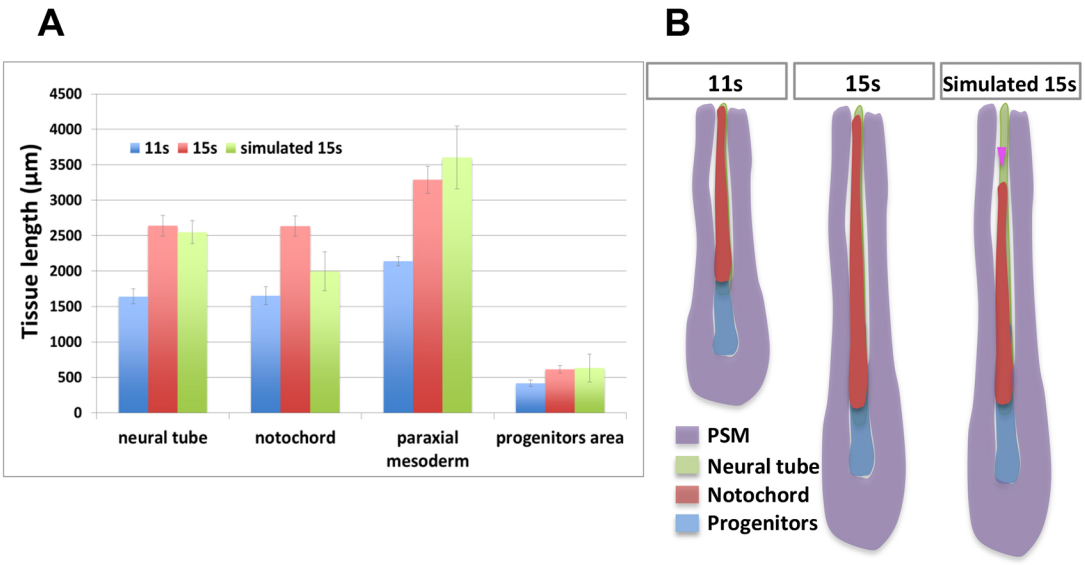

Fig. 4. Computational simulation of multi-tissue proliferation and elongation. Comparison of measured and simulated tissue sizes. Average tissue sizes at 11 s (blue), 15 s (red), simulated by projecting size gain due to tissue-specific proliferation (green) (n=3 embryos by condition). The sizes of the PSM, neural tube and progenitor regions are not significantly different between the measurement at 15 s and the simulation. By contrast, the size of the notochord is different between the measurement at 15 s and the simulation. (B) Schematic of the averaged tissue sizes measured and calculated. Note that in the simulation the notochord is shorter suggesting that there is a sliding between the notochord and the neural tube and paraxial mesoderm (pink arrowhead).

Development (2017) 144, 4462-4472 doi:10.1242/dev.150557

protein Histone-2B-mCherry is driven by the ubiquitous hPGK1 promoter. This transgenic model system allows for visualization of all cells in every tissue by confocal imaging during early embryogenesis (Huss et al., 2015). Because classic confocal techniques did not permit us to image the entire thickness of the tissue from a single direction, we cultured and imaged embryos from both the ventral and dorsal side.

By globally imaging tissue kinetics from the ventral side of the embryo, we observed that various tissues were elongating at different speeds. For example, the paraxial mesoderm elongated faster than the notochord (Movie 1), causing a sliding of the two tissues relative to one another, as predicted by our theoretical model. Additionally, by using a higher magnification for increased *z* resolution and by color-coding the *z* layers we were able to observe differential motion between the endoderm and paraxial mesoderm (Movie 2). In contrast, tissues in the dorsal part of the embryo (neuroectoderm and ectoderm) elongate at a similar rate and fail to display any obvious sliding (Movie 3) movement.

To quantify these diverse tissue kinetics, we developed customized cell-tracking algorithms to determine local differential velocities (detailed in supplementary Materials and Methods). In each tissue, a group of cells located at different positions along the anteroposterior axis (Fig. 5A-C) was tracked, using the last-formed somite as a reference point. The last-formed somite was chosen as a reference because it is visible from both the ventral and dorsal side and we could thus average tissue movements from embryos filmed from either side. Our analysis showed that all tissues elongate compared with the last-formed somite. However, they elongate with different velocity patterns graded along the anteroposterior axis (Fig. 5D). Most tissues (endoderm, ectoderm, lateral plate, notochord) exhibited a weak gradient of velocity (that is, all cells moved at a similar velocity). In contrast, the paraxial mesoderm possesses a very complex behavior with different velocities in its anterior and posterior sections. The velocity of the anterior part was slower than the posterior end, and also below that of all the surrounding tissues, meaning that they dynamically slid past the anterior paraxial mesoderm during elongation. Local velocity in the anterior region became negative, meaning that anterior PSM cells moved closer to the somite and therefore showed tissue compaction. In the posterior part of the PSM, we observed a different behavior: there was a steady increase in PSM velocity until it matched that of the other tissues and began moving in concert in a caudal direction. Taken together, our results reveal an unexpected tissue choreography during axis elongation with tissues sliding relative to one another. Among these tissues, the paraxial mesoderm has a very distinct kinetic of movement suggesting that a particular set of cell behaviors are taking place in this tissue during elongation.

Tissue deformations during embryonic axis elongation

Because we found that axis elongation is defined by differential tissue motions, we wanted to examine intra-tissue deformations to see if they could explain the newly described multi-tissue kinetics. We, therefore, used cell tracking data to compute areas of cell/tissue: (1) rotation (analysis of circular movements in reference to the anteroposterior axis); (2) compression and expansion; and (3) tensors in the elongating embryo (Fig. 6) (detailed in supplementary Materials and Methods).

The rotational analysis gives us insights into large-scale cellular flows taking place in the mediolateral axis of the extending embryo. In the posterior part of the analyzed region, we observed a general medial-to-lateral displacement (Fig. 6A-C, yellow arrowheads; called ‘clockwise’ for the right part of the embryo). These mediolateral movements are reminiscent of gastrulation movements, as cells leave the progenitor zone to intermix with paraxial mesoderm cells. Interestingly, these movements were not only detected at the level of the mesoderm but also in the most dorsal (ectodermal) and most ventral (endodermal) embryonic levels. In the anterior part of the analyzed region, we observed a lateral-to-medial movement (counter-clockwise) of the mesoderm and ectoderm (Fig. 6A,B, red arrowheads). These large movements, which resemble convergence, seem to emerge as a flow of cells rather than as the result of local intercalations. Therefore, we saw a vortex-type motion at the tissue scale, with cells displaced mediolaterally at the level of the tail of the embryo and in a lateral-to-medial direction at the level of the anterior PSM.

To understand better how differential tissue deformations relate to large-scale tissue movements, we created contraction/expansion field maps of the extending embryo (Fig. 6D-F). This analysis showed that most of the dorsal part of the embryo expands except the closing neural tube, which contracts (Fig. 6D, light blue arrowhead). The mesoderm layer (middle layer in the dorsoventral axis) of the embryo behaved differently; the posterior paraxial mesoderm and progenitor region expanded and the more anterior part of the PSM contracted (Fig. 6E,F, pink and white arrowheads, respectively).

To determine the directionality of the observed deformations, we plotted the strain tensors (Fig. 6G-I, Fig. S6). We observed mediolateral contraction where the neural tube is closing (Fig. 6G,G′, Fig. S6). The contraction of the anterior PSM was mainly directed along the mediolateral direction (Fig. 6H,H′, Fig. S6) whereas the posterior expansion was led along the anteroposterior axis (Fig. 6H, H″, Fig. S6). These results were confirmed by analyzing different embryos and other time frames of the movies (data not shown; Movie 4).

Interestingly, rotational movements were correlated with expansion and contraction fields. In particular, lateral-to-medial (counter-clockwise) rotation of the lateral plate and paraxial mesoderm was correlated with compaction in the anterior PSM (Fig. 6B,E, red and white arrowheads) whereas mediolateral (clockwise) movements in the mesoderm were correlated with tissue expansion in the caudal PSM and progenitor region (Fig. 6B, E, yellow and pink arrowheads).

Our approach allowed us to decipher specific intra- and inter-tissue movements in the elongating embryo. Intra-tissue deformations were predominant in the paraxial mesoderm, a tissue that displayed different tissue kinetics from its neighboring tissues (Fig. 5). In the more anterior part of the PSM, we observed a convergent cell flow and contractive behavior correlated with the sliding of surrounding tissues. In contrast, in the posterior part of the PSM and progenitor zone, we observed a clear tissue expansion associated with a correlation in movement with surrounding tissues (Figs 5 and 6).

DISCUSSION

Our volumetric analysis indicates that posterior elongation in an amniote embryo is achieved by complex differential tissue growth. For instance, our results show that the PSM and the neural tube grow more than the neighboring notochord to produce new posterior tissues. The fact that particular cell density is conserved through successive stages suggests that tissue growth is mainly due to the addition of new cells, a fact which is partially confirmed by proliferation data in which we observed that cell cycle time in the PSM and the neural tube is faster than in other tissues such as the notochord. We used H2B-Cherry quail to study cell movements and

Development (2017) 144, 4462-4472 doi:10.1242/dev.150557

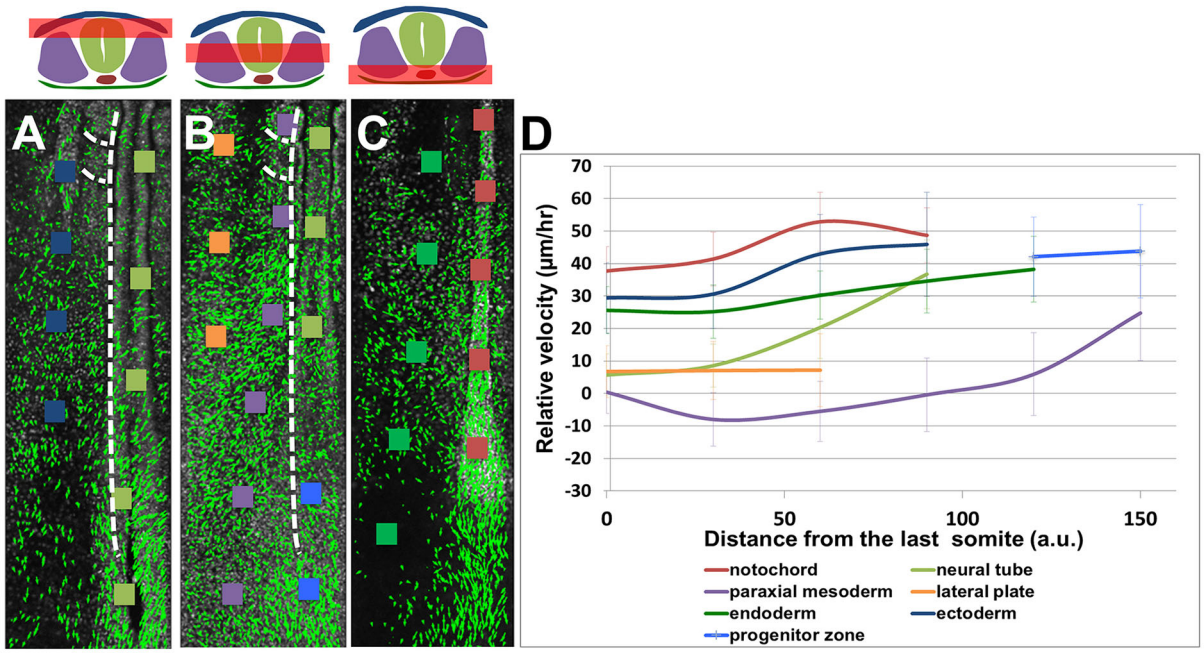

Fig. 5. Analysis of tissue movement and tissue sliding during axis extension. (A-C) Vector field analysis was computed from *PGK1:H2B-Cherry* transgenic embryo time-lapse data: the green arrows represent the average displacement (length in proportional to distance) and direction of tracked cells. The analysis was performed at different dorsoventral levels (symbolized by the red bar on the schema above): dorsal (A), intermediate (B) and ventral (C). Colored squares represent examples of zones in different tissues along the A/P axis in which the analysis has been carried out (purple for paraxial mesoderm, the notochord is red, the neural tube is light green, ectoderm is dark blue, endoderm is dark green, lateral plate is orange, progenitor region is light blue). The horizontal dashed lines indicate the inter-somitic space and the vertical dashed lines indicate the limit between neural tube and paraxial mesoderm. (D) Averaged differential tissue motilities along the A/P axis. Zones of interest (squares in A-C) were tracked, and their motilities were calculated compared with the last-formed somite. *n*=3 and 2 embryos from the ventral and dorsal sides, respectively. Error bars represent s.e.m. Distances from the last-formed somite to the end of the notochord were normalized. a.u., arbitrary units. Time-lapse raw data corresponding to representative embryos shown here are available in the Dryad Digital Repository (Bénazéraf et al., 2017).

tissue deformations during axis elongation because this method offers the possibility to dynamically image every cell in all tissues. Our analysis shows that tissues slide along each other during the elongation process. In particular, differential tissue motion is prominent at the level of the anterior PSM as other tissues slide past the PSM in the caudal direction. Tissue deformation analysis shows that caudal expansion of the PSM tissues is correlated with mediolateral rotational movements and that tissue compression in the anterior PSM tissues is correlated with lateral-to-medial convergent movements. Owing to the active role of the PSM in axis extension (Bénazéraf et al., 2010), it is tempting to speculate that its deformations (due to proliferation/addition of cells and migration) could contribute to the coordinated motions of neighboring tissues (model in Fig. 7). In the most posterior part of the embryo, the anteroposterior expansion of the PSM might drive the elongation by stretching the surrounding tissues. In more anterior regions the scenario is different: the PSM tissue contracts and get compacted whereas surrounding tissues could follow the posterior stretch/elongation imposed by the caudal PSM. The difference in behavior between anterior PSM and surrounding tissues could be reflected in the tissue sliding that we observed. In the future, it would be interesting to test this model by mechanically interfering with the forces generated within the PSM and analyzing the effects on the deformations of surrounding tissues.

Time-lapse imaging of transgenic avian embryos is an emerging model system in which to study early morphogenesis events. In particular, the recent development of novel transgenic lines has allowed the unraveling of several aspects of early axis formation. Using a transgenic chicken ubiquitously expressing membrane-GFP it has been shown that cell intercalation and cell division drive anteroposterior extension of the primitive streak (Firmino et al., 2016; Rozbicki et al., 2015). These studies focus mainly on following cell movements in the epiblast, which is a relatively flat epithelium composed of a single cell layer. To study axis elongation at later stages, we needed to use a model system in which we could track cells having very different shapes, located in various tissues (epithelial, pseudo-epithelial or mesenchymal) at different dorsal-ventral levels of the developing embryo. We chose to use confocal imaging of transgenic quail expressing H2B-chFP to label the relatively uniform-shaped nucleus and we specifically designed image treatment software that allowed for analysis of cell movement in different tissues simultaneously. Morphogenetic collective cell movements and tissue deformations are crucial aspects of embryonic morphogenesis. Here, we demonstrate that the combination of transgenic quail time-lapse imaging and image analysis allowed us to quantify these movements and deformations at the multi-tissue scale.

Our data on the volumetric contribution to axis extension suggest that the PSM is the main contributor in quail axis extension. These data are consistent with previous tissue-ablation experiments showing that the PSM is central to axis extension in the chicken embryo (Bénazéraf et al., 2010). In a recent study, it has been demonstrated that zebrafish posterior elongation is mainly due to convergence rather than posterior volumetric growth, in contrast to mouse embryos (Steventon et al., 2016). This study also points out that the zebrafish PSM region grows much less in comparison with

Development (2017) 144, 4462-4472 doi:10.1242/dev.150557

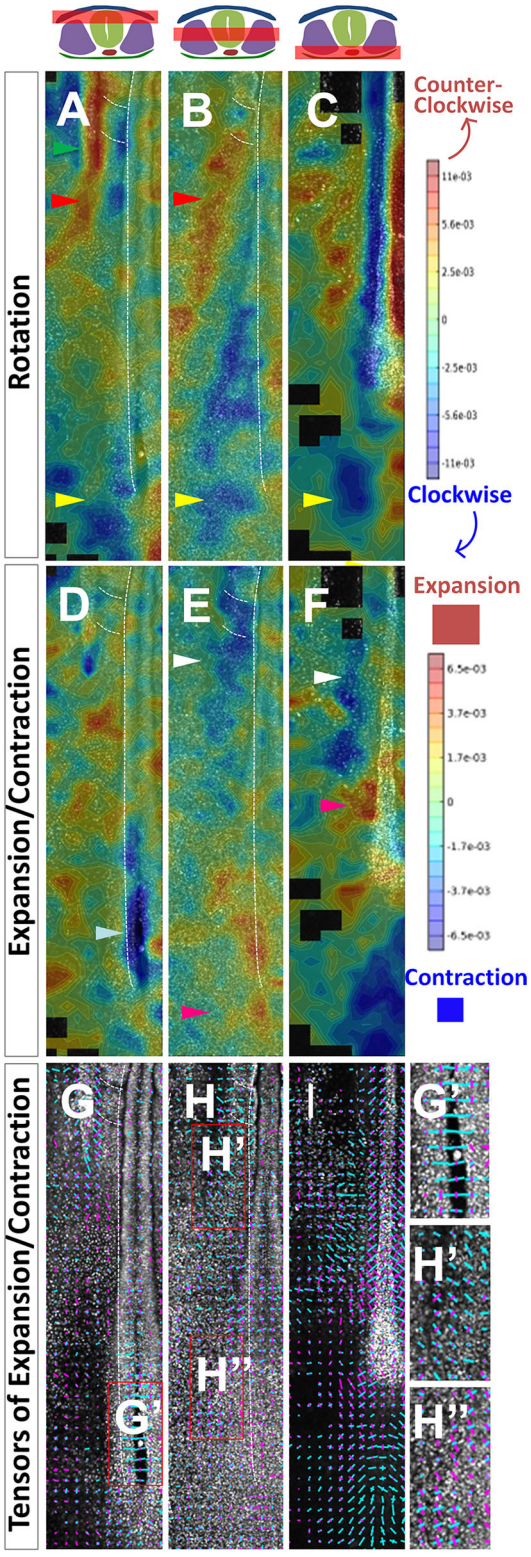

Fig. 6. Tissue deformation analysis during axis extension. Rotational analysis (A-C), expansion/contraction (D-F) and tensor maps (G-I) were computed from 3D cell-tracking data at different dorsoventral levels from representative embryos: (A,D,G) represents the most ventral level, (B,E,H) intermediate level, (C,F,I) the most dorsal level. In the rotational analysis (A-C), the angle of rotations are color-coded: blue represents the clockwise rotation, red the counter-clockwise rotation. Note that we can see medial-to-lateral movement in the caudal intermediate part (yellow arrowheads in A-C) and medial-to-lateral rotation in the anterior intermediate part (red arrowheads in A, B); note that we also detect sliding at the boundaries between tissues in this analysis (green arrowhead in A shows the intermediate mesoderm sliding in between the somites and the lateral mesoderm). In the compaction/expansion map (D-F), contraction and expansion field are color-coded, red representing an expansion and blue a compaction. Note the expansion in the caudal intermediate and ventral level (pink arrowheads in E,F), and the contraction in the anterior level, and the neural tube closure (white and light blue arrowheads). In the tensors analysis (G-I), the compaction values are presented in blue and the expansion values in pink, intensities are represented by length and directionality by their orientation. G′,H′ and H″ are high-magnification views of the boxed areas in G and H. Note that the expansion of the caudal ventral region of the embryo has a strong elongation component (A/P axis) (H″) whereas the contractions in the anterior part of the PSM (H′), or in the caudal neural tube (G′) are mainly due to convergence (mediolateral contraction) (see also Fig. S6 for tensor maps without the embryo image). Black areas represent the area with insufficient number of cells to perform a statistically significant analysis. Time-lapse raw data corresponding to representative embryos shown here are available in the Dryad Digital Repository (Bénazéraf et al., 2017).

other tissues such as the neural tube, a situation that is very different from that in the bird embryo, in which PSM growth is an important part of the overall posterior growth. Therefore, axis extension seems to be regulated by different tissue-specific behaviors in different species. The slower growth of zebrafish posterior tissue could be related to the fact that the cell cycle appears to slow down in S phase and at the G2/M transition in axial progenitors or in G1 phase for the caudal notochord cells (Bouldin et al., 2014; Sugiyama et al., 2014, 2009). Therefore, although zebrafish and quail might have different tissue-specific elongation mechanisms, the slowing down of the cell cycle in the caudal notochord cells seems to be evolutionarily conserved between these species. We have previously shown that global treatment of the chick embryo with cell cycle inhibitors does not alter cellular movements in the PSM (Bénazéraf et al., 2010). However, we did not assess tissue volumetric changes in those experiments. Our present study suggests a crucial role for differential proliferation in tissue kinetics and volumetric growth. Volumetric changes of the different tissues of the posterior part of the embryo in the context of local or global cell cycle inhibition will, therefore, be essential to functionally assess the role of proliferation in tissue kinetics and axial extension in different species.

Cell mixing in the caudal PSM has been documented extensively in the chicken embryo (Bénazéraf et al., 2010; Delfini et al., 2005; Kulesa and Fraser, 2002; Stern et al., 1988) and is also visible in the elongating quail embryo in our study (Movies 1 and 2). In the present study, we have quantified tissue deformations and observed that the PSM displays extensive expansion in its posterior part (where cells move extensively) and contraction in the anterior part (where cell movement diminishes). These deformations are also consistent with the caudo-rostral increasing cell density gradient measured in the PSM. The origins of the forces that trigger compaction have not been identified; they could be coming directly from the cells located anteriorly and/or they could be an indirect effect of long-distance forces generated by posterior expansion or the convergence of lateral tissue. The caudal expansion of the paraxial tissue could also result from the integration of different phenomena: (1) the gradient of cell random migration, which disperses and reorganizes PSM cells; (2) new cells coming from proliferation (as PSM is actively proliferating in quail); and, finally (3), from new cells migrating from the progenitor region (as shown in the rotational analysis). The regulation of the latter has been shown to be an important factor in slowing the elongation process and therefore regulating the size of the body

Development (2017) 144, 4462-4472 doi:10.1242/dev.150557

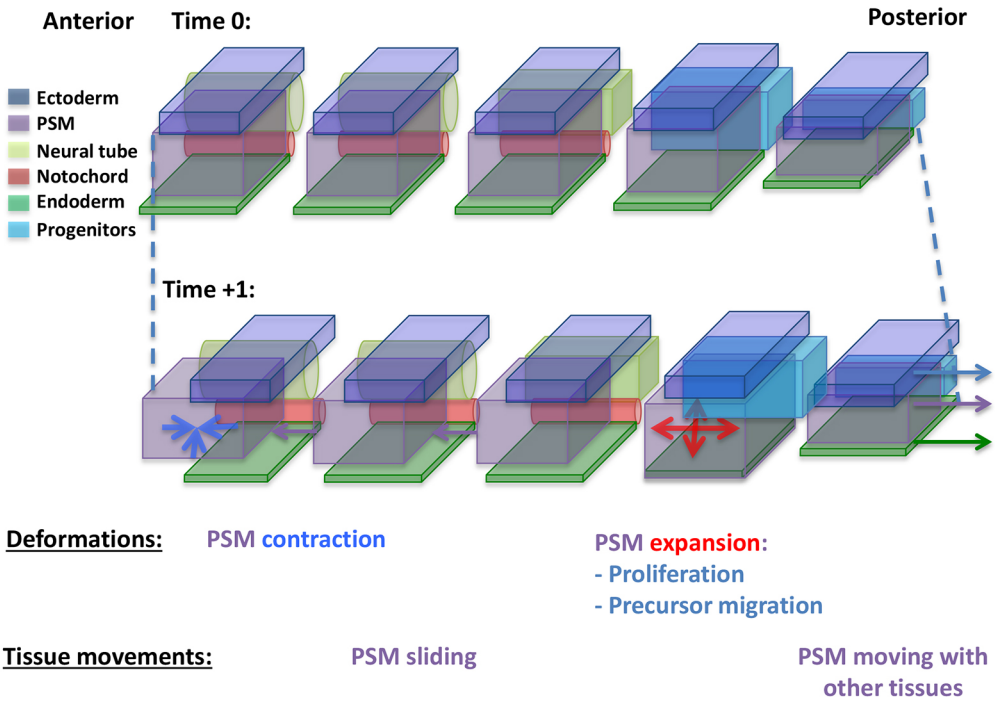

Fig. 7. Model of multi-tissue axis elongation kinetics. Multi-tissue movements at different anteroposterior levels and time points showing relative movements of the different tissues. Posterior tissues of one side of the embryo are represented from the lateral view: anterior to the left, posterior to the right; paraxial mesoderm is purple, the notochord is red, the neural tube is light green, ectoderm is dark blue, endoderm is dark green). The tissue is shown in sections to highlight their differential motions between time 0 and time +1 (e.g. compare relative positions of PSM and surrounding tissues between time 0 and time +1). PSM deformations are marked with blue (compression) and red (expansion) arrows. Tissue directional movement is shown by colored arrows: purple for the PSM, blue for ectoderm/progenitors and dark green for endoderm. Main tissue movements and deformations are described below the schemes with a color code corresponding to tissue identity. High proliferation in the PSM and migration in the caudal PSM is correlated with local tissue expansion. Compression is taking place in the anterior PSM. The pattern of posterior-expansion/anterior-contraction is linked with the PSM vortex movement. Posterior PSM expands, moving posteriorly with neighboring tissues (light blue, purple and green arrows on the right part of the time +1 schema). Axial tissues located more anteriorly (notochord and neural tube) follow this caudal movement and move much faster than the adjacent contracting PSM located anteriorly to the expansion zone. This differential behavior in the PSM tissue could create (a putative aspect of the model) the axial/paraxial tissue sliding with the PSM sliding anteriorly compared with the other tissues (purple arrows pointing to the left on time +1 schema).

(Denans et al., 2015; Gomez et al., 2008; Iimura and Pourquié, 2006). These mediolateral rotational movements that we observed in the caudal part of the embryo are accompanied by lateral-to-medial movement at the level of the anterior PSM. These movements, also observed at comparable stages in the chicken embryo, form large-scale tissue motions as they also involve the extracellular matrix (ECM) (Bénazéraf et al., 2010). The extent of their contributions to posterior axis extension compared with the anteroposterior increasing gradient of tissue expansion is still to be investigated. Interestingly, they could reflect the continuation of existing movements that have been observed during earlier phases of bird development and proposed to be central in early axis extension (Yang et al., 2002; Fleury et al., 2015).

In this study, we analyze tissue movements and deformations during amniote axis elongation. Interestingly, the paraxial mesoderm seems to have the most singular behavior compared with other tissues as it contracts anteriorly and expands posteriorly and therefore extends differentially from other tissues. Paraxial mesoderm is covered by ECM matrix containing proteins such as fibrillin 2 and fibronectin (Czirók et al., 2004; Martins et al., 2009; Bénazéraf et al., 2010; Rifes and Thorsteinsdóttir, 2012). We observed that the fibronectin movement is correlated more with the PSM cell movements than with other tissues (data not shown). This surrounding layer of ECM might, therefore, be important for keeping a physical separation between the tissues and for allowing tissue sliding to occur and/or for transmitting forces when tissues are moving together (Araya et al., 2016). In particular, potential mechanical tissue coupling in the most posterior part of the embryo and mechanical tissue decoupling where tissue slides relative to each other (Fig. 7) could be regulated by different physical properties of the tissues and ECM molecules at the interface between tissues. Data obtained in mouse and zebrafish show that integrin, which is a molecular link between ECM and cells, is required for tissue elongation and tissue mechanics (Girós et al., 2011; Dray et al., 2013). Interestingly, and in agreement with our measures of cell density and tissue deformation in amniotes, biophysical measurements performed in zebrafish PSM tissue show that this tissue is stiff anteriorly and more fluid posteriorly (Serwane et al., 2017). This posterior fluidity within the PSM could allow tissue expansion and force generation to deform other tissues. The difference in the nature of the forces created at the interface between the PSM tissue and the matrix or the others tissues at different A/P axis positions might be of importance in generating the tissue kinetics that we observed. Future studies in which we can measure forces exerted between tissues will be of great significance to precisely identify and localize the different factors defining multi-tissue elongation.

MATERIALS AND METHODS

Ethics statement

All experimental methods and animal husbandry procedures were performed following the guidelines of the National Institutes of Health and with the approval of the Institutional Animal Care and Use Committee at

Development (2017) 144, 4462-4472 doi:10.1242/dev.150557

the California Institute of Technology, the University of Southern California (USC), and Children's Hospital Los Angeles.

Quail embryo and embryo culture

Wild-type quail embryos (*Coturnix japonica*) were obtained from commercial sources (AA Lab Eggs, Westminster, CA, USA) and the USC aviary. The *PGK1:H2B-chFP* quail line generation was described previously (Huss et al., 2015) and is maintained in the USC aviary. Embryos were staged according to Ainsworth et al. (2010) and Hamburger and Hamilton (1992). Embryos were cultured *ex ovo* with filter paper on albumen agar plates according to the EC (early chick) technique (Chapman et al., 2001).

Staining and immunodetection

Embryos were collected at the desired stages and fixed overnight in 4% formaldehyde [36% formaldehyde (Sigma Aldrich, 47608) diluted to 4% in PBS]. Blocking and tissue permeabilization was carried out for 2 h in PBS/0.5% Triton X-100/1% donkey serum. Primary antibodies against Sox2 (1/5000, EMD Millipore, ab5603) and Bra (1/500, R&D Systems, AF2085) were incubated overnight at 4°C. After washing off primary antibody in PBT (PBS/0.1% Triton X-100), embryos were incubated with secondary antibodies [donkey anti-rabbit IgG Alexa Fluor 488 (A21206) and donkey anti-goat IgG Alexa Fluor 594 (A11058), 1/1000, Thermo Fisher Scientific] and DAPI (1/1000, Thermo Fisher Scientific, D1306) overnight at 4°C. The embryos were washed in PBT, cleared in U2 scale solution (Hama et al., 2011) for at least 48 h at 4°C and then mounted between a slide and coverslip and imaged by confocal/two-photon microscopy.

Proliferation and apoptosis analysis

Proliferation was assessed by EdU staining. EdU (Click-iT EdU Alexa Fluor 488 Imaging Kit, Thermo Fisher Scientific, C10337) was diluted in PBS to obtain a 10 mM stock solution. Fifty microliters of working solution (500 µM) was dropped every 2 h onto cultured embryos. Stage 10 HH embryos were incubated for 3, 6 and 9 h with the EdU, then washed with PBS and fixed in 4% formaldehyde as described above. Apoptosis was assessed using the TUNEL kit (Click-iT Plus TUNEL assay Alexa Fluor 594, Thermo Fisher Scientific, C10618) after embryo fixation according to the manufacturer's instructions. EdU- or TUNEL-stained embryos were co-stained with DAPI cleared in U2 scale solution for at least 48 h at 4°C and then mounted and imaged by confocal/two-photon microscopy.

Imaging

Quail embryos were collected at desired stages (10 to 11 HH) with a paper filter as described before (Chapman et al., 2001), washed in PBS and either fixed directly in formaldehyde solutions (see above) or cultured on agar albumen plates for EdU incorporation or time-lapse imaging. For fixed-tissue imaging, embryos were mounted between slide and coverslip, separated by a layer of electrical tape. For live-imaging experiments, embryos were cultured at 37ºC in culture imaging chambers (Lab Tek chambered #1 coverglass slide, Thermo Fisher Scientific) pre-coated with a mix of albumen agar (Chapman et al., 2001) . Embryos were imaged using an inverted 780 Zeiss microscope using confocal or two-photon excitation with 10×/0.45, 20×/0.8 or 25×/0.8 objectives. DAPI (405 nm) and EdU (488 nm) fluorescent signals were separated using the two-photon online fingerprinting function in ZEN 2011 software (http://zeiss-campus.magnet.fsu.edu/tutorials/spectralimaging/lambdastack/indexflash.html). For time-lapse imaging, several adjacent *xyz* fields of view were stitched together post-collection. Images were taken every 5-10 µm in the *z* axis with a time resolution ranging from 5 to 6 min.

Image analysis

Tissue volumes were hand drawn, rendered and volumetric values were calculated using Imaris software (Bitplane). The Spot function of Imaris was used to localize nuclei in the 3D image data set (collected from DAPI-stained embryos) and to extract nuclei coordinates (*x*,*y*,*z*). Cell densities were calculated using a variation of k nearest neighbor algorithm (see supplementary Materials and Methods). The number of EdU- or TUNEL-positive cells and -negative cells (stained by DAPI only) was determined by using the Spot function of Imaris. Cell cycle length was determined using described methods (Nowakowski et al., 1989) (see supplementary Materials and Methods for details). New tracking algorithms were designed based on image treatment, nuclei detection, cross-correlation and multi-cellular matching between consecutive frames (see supplementary Materials and Methods). For measurement comparisons, a statistical *t*-test (two tailed) was used. Tissue-movement analysis was computed from cell-tracking data after flow regularization (using minimization of some energy function). This regularization permits the computation of deformation tensors and allowed us to quantify tissue tectonics (see supplementary Materials and Methods). Movies were edited using Adobe Premiere, FIJI, and Zeiss ZEN black software.

Acknowledgements

We thank Daniela Roellig, Alexis Hubaud, Gonçalo Neto, Ben Steventon, Constance Wu and Guillaume Allio for critically reading the manuscript or helping with the figures. We also thank members of the Rusty Lansford, Scott Fraser, Olivier Pourquié and Paul François teams for suggestions and stimulating discussions during the project.

Competing interests

The authors declare no competing or financial interests.

Author contributions

Conceptualization: B.B., P.F., R.L., O.P.; Methodology: B.B., M.B., M.T., D.H., R.L.; Software: M.B., M.T., T.S, Amelia Shirtz, Andrew Shirtz, P.F.; Validation: B.B., M.B; M.T.; Formal analysis: B.B., M.B. ; Investigation: B.B., M.B., M.T., A.W., T.S., Amelia Shirtz, Andrew Shirtz; Resources: B.B., M.B, M.T., A.W., T.S., Amelia Shirtz, Andrew Shirtz, D.H., P.F., R.L.; Data curation: B.B., M.B., A.W., T.S., Amelia Shirtz, Andrew Shirtz; Writing - original draft: B.B.; Writing - review & editing: B.B., D. H., O. P., P.F., R.L.; Visualization: B.B., M.B. T.S.; Supervision: B.B., P.F., R.L.; Project administration: B.B., P.F., R.L.; Funding acquisition: B.B., O.P., P.F., R.L.

Funding

This work was supported by a Human Frontier Science Program grant (RGP0051 to O.P., R.L., P.F.).

Data availability

Time-lapse raw data corresponding to representative embryos analyzed in Figs 5 and 6 are available in the Dryad Digital Repository (Bénazéraf et al., 2017): http://dx.doi.org/10.5061/dryad.4g1h2.

Supplementary information

Supplementary information available online at
http://dev.biologists.org/lookup/doi/10.1242/dev.150557.supplemental

References

Ainsworth, S. J., Stanley, R. L. and Evans, D. J. R. (2010). Developmental stages of the Japanese quail. *J. Anat.* **216**, 3-15.

Araya, C., Carmona-Fontaine, C. and Clarke, J. D. W. (2016). Extracellular matrix couples the convergence movements of mesoderm and neural plate during the early stages of neurulation. *Dev. Dyn.* **245**, 580-589.

Bénazéraf, B., Francois, P., Baker, R. E., Denans, N., Little, C. D. and Pourquié, O. (2010). A random cell motility gradient downstream of FGF controls elongation of an amniote embryo. *Nature* **466**, 248-252.

Bénazéraf, B., Beaupeux, M., Tcherknookov, M., Wallingford, A., Salisbury, T., Shirtz, A. Huss, D. Pourquié, O., François, P. and Lansford, R. (2017). Data from: Multi-scale quantification of tissue behavior during amniote embryo axis elongation. *Dryad Digital Repository*, doi:10.5061/dryad.4g1h2.

Blanchard, G. B., Kabla, A. J., Schultz, N. L., Butler, L. C., Sanson, B., Gorfinkiel, N., Mahadevan, L. and Adams, R. J. (2009). Tissue tectonics: morphogenetic strain rates, cell shape change and intercalation. *Nat. Methods* **6**, 458-464.

Bouldin, C. M., Snelson, C. D., Farr, G. H. and Kimelman, D. (2014). Restricted expression of cdc25a in the tailbud is essential for formation of the zebrafish posterior body. *Genes Dev.* **28**, 384-395.

Chapman, S. C., Collignon, J., Schoenwolf, G. C. and Lumsden, A. (2001). Improved method for chick whole-embryo culture using a filter paper carrier. *Dev. Dyn.* **220**, 284-289.

Czirók, A., Rongish, B. J. and Little, C. D. (2004). Extracellular matrix dynamics during vertebrate axis formation. *Dev. Biol.* **268**, 111-122.

Delfini, M.-C., Dubrulle, J., Malapert, P., Chal, J. and Pourquié, O. (2005). Control of the segmentation process by graded MAPK/ERK activation in the chick embryo. *Proc. Natl. Acad. Sci. USA* **102**, 11343-11348.
Denans, N., Iimura, T. and Pourquié, O. (2015). Hox genes control vertebrate body elongation by collinear Wnt repression. *eLife* **4**.
Dray, N., Lawton, A., Nandi, A., Jülich, D., Emonet, T. and Holley, S. A. (2013). Cell-fibronectin interactions propel vertebrate trunk elongation via tissue mechanics. *Curr. Biol.* **23**, 1335-1341.
Firmino, J., Rocancourt, D., Saadaoui, M., Moreau, C. and Gros, J. (2016). Cell division drives epithelial cell rearrangements during gastrulation in chick. *Dev. Cell* **36**, 249-261.
Fleury, V., Chevalier, N. R., Furfaro, F. and Duband, J.-L. (2015). Buckling along boundaries of elastic contrast as a mechanism for early vertebrate morphogenesis. *Eur. Phys. J. E Soft. Matter* **38**, 92.
Girós, A., Grgur, K., Gossler, A. and Costell, M. (2011). α5β1 integrin-mediated adhesion to fibronectin is required for axis elongation and somitogenesis in mice. *PLoS ONE* **6**, e22002.
Gomez, C., Özbudak, E. M., Wunderlich, J., Baumann, D., Lewis, J. and Pourquié, O. (2008). Control of segment number in vertebrate embryos. *Nature* **454**, 335-339.
Hama, H., Kurokawa, H., Kawano, H., Ando, R., Shimogori, T., Noda, H., Fukami, K., Sakaue-Sawano, A. and Miyawaki, A. (2011). Scale: a chemical approach for fluorescence imaging and reconstruction of transparent mouse brain. *Nat. Neurosci.* **14**, 1481-1488.
Hamburger, V. and Hamilton, H. L. (1992). A series of normal stages in the development of the chick embryo. 1951. *Dev. Dyn.* **195**, 231-272.
Huss, D., Benazeraf, B., Wallingford, A., Filla, M., Yang, J., Fraser, S. E. and Lansford, R. (2015). A transgenic quail model that enables dynamic imaging of amniote embryogenesis. *Development* **142**, 2850-2859.
Iimura, T. and Pourquié, O. (2006). Collinear activation of Hoxb genes during gastrulation is linked to mesoderm cell ingression. *Nature* **442**, 568-571.
Keller, R., Cooper, M. S., Danilchik, M., Tibbetts, P. and Wilson, P. A. (1989). Cell intercalation during notochord development in Xenopus laevis. *J. Exp. Zool.* **251**, 134-154.
Kulesa, P. M. and Fraser, S. E. (2002). Cell dynamics during somite boundary formation revealed by time-lapse analysis. *Science* **298**, 991-995.
Lawson, A. and Schoenwolf, G. C. (2001). New insights into critical events of avian gastrulation. *Anat. Rec.* **262**, 238-252.
Lawton, A. K., Nandi, A., Stulberg, M. J., Dray, N., Sneddon, M. W., Pontius, W., Emonet, T. and Holley, S. A. (2013). Regulated tissue fluidity steers zebrafish body elongation. *Development* **140**, 573-582.
Li, Y., Trivedi, V., Truong, T. V., Koos, D. S., Lansford, R., Chuong, C.-M., Warburton, D., Moats, R. A. and Fraser, S. E. (2015). Dynamic imaging of the growth plate cartilage reveals multiple contributors to skeletal morphogenesis. *Nat. Commun.* **6**, 6798.
Martins, G. G., Rifes, P., Amândio, R., Rodrigues, G., Palmeirim, I. and Thorsteinsdóttir, S. (2009). Dynamic 3D cell rearrangements guided by a fibronectin matrix underlie somitogenesis. *PLoS ONE* **4**, e7429.
Nowakowski, R. S., Lewin, S. B. and Miller, M. W. (1989). Bromodeoxyuridine immunohistochemical determination of the lengths of the cell cycle and the DNA-synthetic phase for an anatomically defined population. *J. Neurocytol.* **18**, 311-318.
Olivera-Martinez, I., Harada, H., Halley, P. A. and Storey, K. G. (2012). Loss of FGF-dependent mesoderm identity and rise of endogenous retinoid signalling determine cessation of body axis elongation. *PLoS Biol.* **10**, e1001415.
Rauzi, M., Krzic, U., Saunders, T. E., Krajnc, M., Ziherl, P., Hufnagel, L. and Leptin, M. (2015). Embryo-scale tissue mechanics during Drosophila gastrulation movements. *Nat. Commun.* **6**, 8677.
Rifes, P. and Thorsteinsdóttir, S. (2012). Extracellular matrix assembly and 3D organization during paraxial mesoderm development in the chick embryo. *Dev. Biol.* **368**, 370-381.
Rozbicki, E., Chuai, M., Karjalainen, A. I., Song, F., Sang, H. M., Martin, R., Knölker, H.-J., MacDonald, M. P. and Weijer, C. J. (2015). Myosin-II-mediated cell shape changes and cell intercalation contribute to primitive streak formation. *Nat. Cell Biol.* **17**, 397-408.
Serwane, F., Mongera, A., Rowghanian, P., Kealhofer, D. A., Lucio, A. A., Hockenbery, Z. M. and Campàs, O. (2017). In vivo quantification of spatially varying mechanical properties in developing tissues. *Nat. Methods* **14**, 181-186.
Shih, J. and Keller, R. (1992a). Cell motility driving mediolateral intercalation in explants of Xenopus laevis. *Development* **116**, 901-914.
Shih, J. and Keller, R. (1992b). Patterns of cell motility in the organizer and dorsal mesoderm of Xenopus laevis. *Development* **116**, 915-930.
Stern, C. D., Fraser, S. E., Keynes, R. J. and Primmett, D. R. (1988). A cell lineage analysis of segmentation in the chick embryo. *Development* **104** Suppl., 231-244.
Steventon, B., Duarte, F., Lagadec, R., Mazan, S., Nicolas, J.-F. and Hirsinger, E. (2016). Species-specific contribution of volumetric growth and tissue convergence to posterior body elongation in vertebrates. *Development* **143**, 1732-1741.
Sugiyama, M., Sakaue-Sawano, A., Iimura, T., Fukami, K., Kitaguchi, T., Kawakami, K., Okamoto, H., Higashijima, S.-I. and Miyawaki, A. (2009). Illuminating cell-cycle progression in the developing zebrafish embryo. *Proc. Natl. Acad. Sci. USA* **106**, 20812-20817.
Sugiyama, M., Saitou, T., Kurokawa, H., Sakaue-Sawano, A., Imamura, T., Miyawaki, A. and Iimura, T. (2014). Live imaging-based model selection reveals periodic regulation of the stochastic G1/S phase transition in vertebrate axial development. *PLoS Comput. Biol.* **10**, e1003957.
Tenin, G., Wright, D., Ferjentsik, Z., Bone, R., McGrew, M. J. and Maroto, M. (2010). The chick somitogenesis oscillator is arrested before all paraxial mesoderm is segmented into somites. *BMC Dev. Biol.* **10**, 24.
Warga, R. M. and Kimmel, C. B. (1990). Cell movements during epiboly and gastrulation in zebrafish. *Development* **108**, 569-580.
Warren, M., Puskarczyk, K. and Chapman, S. C. (2009). Chick embryo proliferation studies using EdU labeling. *Dev. Dyn.* **238**, 944-949.
Yang, X., Dormann, D., Münsterberg, A. E. and Weijer, C. J. (2002). Cell movement patterns during gastrulation in the chick are controlled by positive and negative chemotaxis mediated by FGF4 and FGF8. *Dev. Cell* **3**, 425-437.
Ybot-Gonzalez, P., Savery, D., Gerrelli, D., Signore, M., Mitchell, C. E., Faux, C. H., Greene, N. D. E. and Copp, A. J. (2007). Convergent extension, planar-cell-polarity signalling and initiation of mouse neural tube closure. *Development* **134**, 789-799.

Supplemental Figures

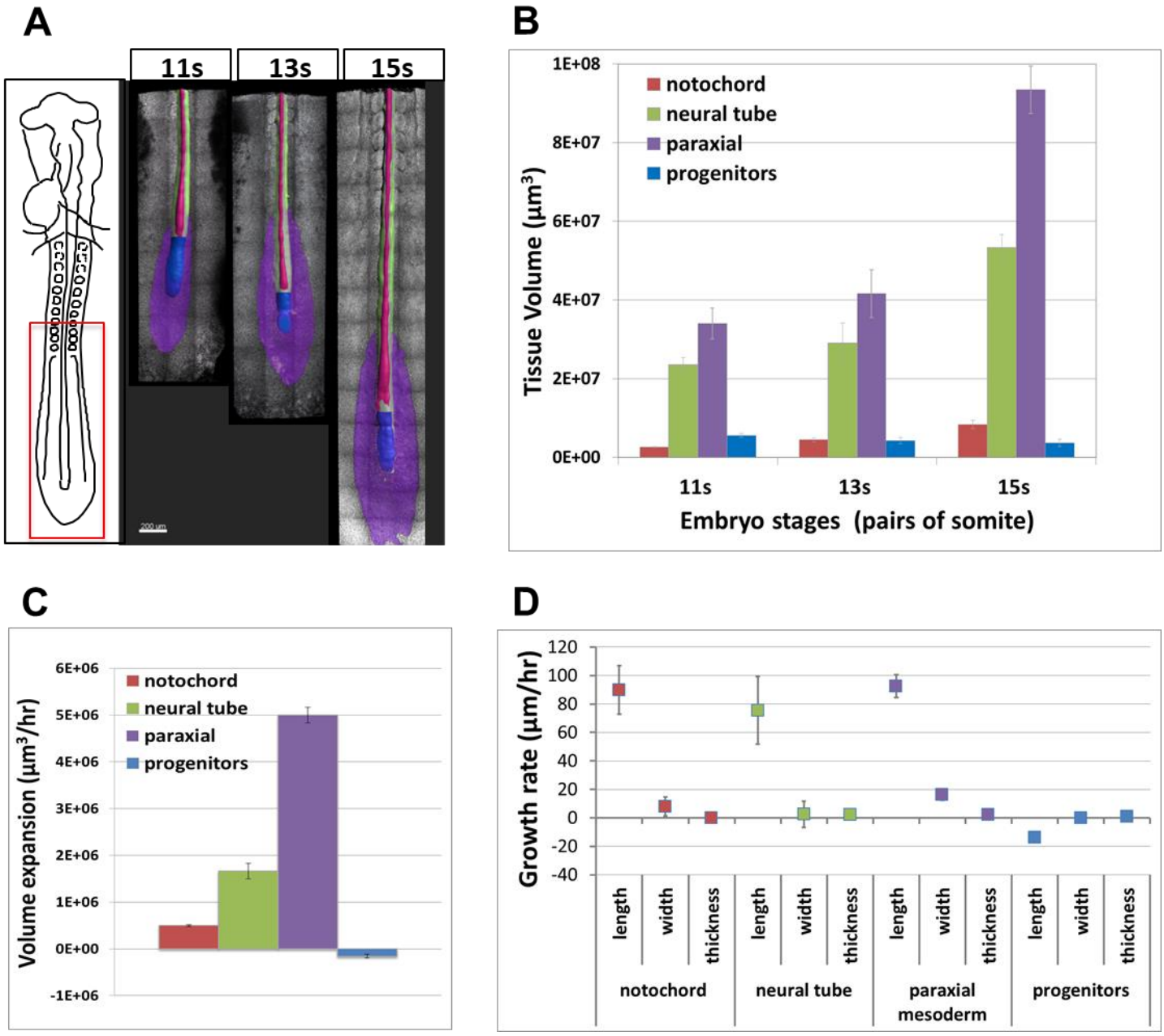

Supplemental Figure 1: Tissue volume growth during axis extension after immunostaining (associated to figure1).

A) 3D representation of different tissues after immuno-detection of Sox2 and Bra during axis extension. The sample on the left is a representative 11 pairs of somite embryo, the sample in the middle is a 13 pairs of somites embryo, and the sample at the right is a 15 pairs of somite embryo. Red is the notochord (High Brachyury expression), purple is the caudal paraxial mesoderm (low Brachyury expression), Blue is the progenitor zone (co-expression of Sox2 and Brachyury), and green is the neural tissue (Sox2 positive). B) Tissue volume measurement for the different stages of development (n=3 embryo per

stage). C) Rate of tissue expansion for the different tissue over time (μm^3/hr). r^2 is calculated for the linear regression of the slope. D) Rate of tissue expansion for the different tissue in the different dimensions (*x*,*y*,*z*) over time (μm/hr). Errors bars are standard errors of the mean. Using this method we were able to distinguish different rates of growth based on specific protein expression domains. The caudal paraxial mesoderm (Bra low) has a higher growth rate than any other tissue: $5x10^6$ μm^3/hr. The neural tube increased its volume at a rate of $1x10^6$ μm^3/hr whereas the notochord increased at a volume of $5x10^5$ μm^3/hr and the progenitor zone shrank at a rate of $1.57x10^5$ μm^3/hr (n =4 embryo/ stages).

A

	axial pro	lat plate	lat plate pro	neural tube	notochord	paraxial pro	psm
axial pro	-	0.0089	0.5688	0.0001	0.0191	0.0099	0.7514
lat plate	-	-	0.0464	0.0050	0.4526	0.0000	0.0001
lat plate pro	-	-	-	0.0003	0.0496	0.0033	0.3334
neural tube	-	-	-	-	0.0714	0.0000	0.0001
notochord	-	-	-	-	-	0.0002	0.0098
paraxial pro	-	-	-	-	-	-	0.0066
psm	-	-	-	-	-	-	-

B

11s vs 13s

	axial pro	lat plate	ectoderm	neural tube	notochord	endoderm	psm
axial pro	0.3097	-	-	-	-	-	-
lat plate	-	0.4560	-	-	-	-	-
ectoderm	-	-	0.3757	-	-	-	-
neural tube	-	-	-	0.3916	-	-	-
notochord	-	-	-	-	0.1979	-	-
endoderm	-	-	-	-	-	0.0187	-
psm	-	-	-	-	-	-	0.0892

11s vs 15s

	axial pro	lat plate	ectoderm	neural tube	notochord	endoderm	psm
axial pro	0.8333	-	-	-	-	-	-
lat plate	-	0.0200	-	-	-	-	-
ectoderm	-	-	0.0183	-	-	-	-
neural tube	-	-	-	0.0805	-	-	-
notochord	-	-	-	-	0.2648	-	-
endoderm	-	-	-	-	-	0.1404	-
psm	-	-	-	-	-	-	0.5010

13s vs 15s

	axial pro	lat plate	ectoderm	neural tube	notochord	endoderm	psm
axial pro	0.7117	-	-	-	-	-	-
lat plate	-	0.0572	-	-	-	-	-
ectoderm	-	-	0.0585	-	-	-	-
neural tube	-	-	-	0.0361	-	-	-
notochord	-	-	-	-	0.8510	-	-
endoderm	-	-	-	-	-	0.0624	-
psm	-	-	-	-	-	-	0.1345

Supplemental Figure 2: Statistical analysis of average cell densities (associated to Figure 2).

A) Comparison between tissues n=9. B) Comparison between stages n=3. Average densities have been statistically compared by t-test (two tailed), highlights show conditions in which the differences in densities are statistically different ($p<0.05$)

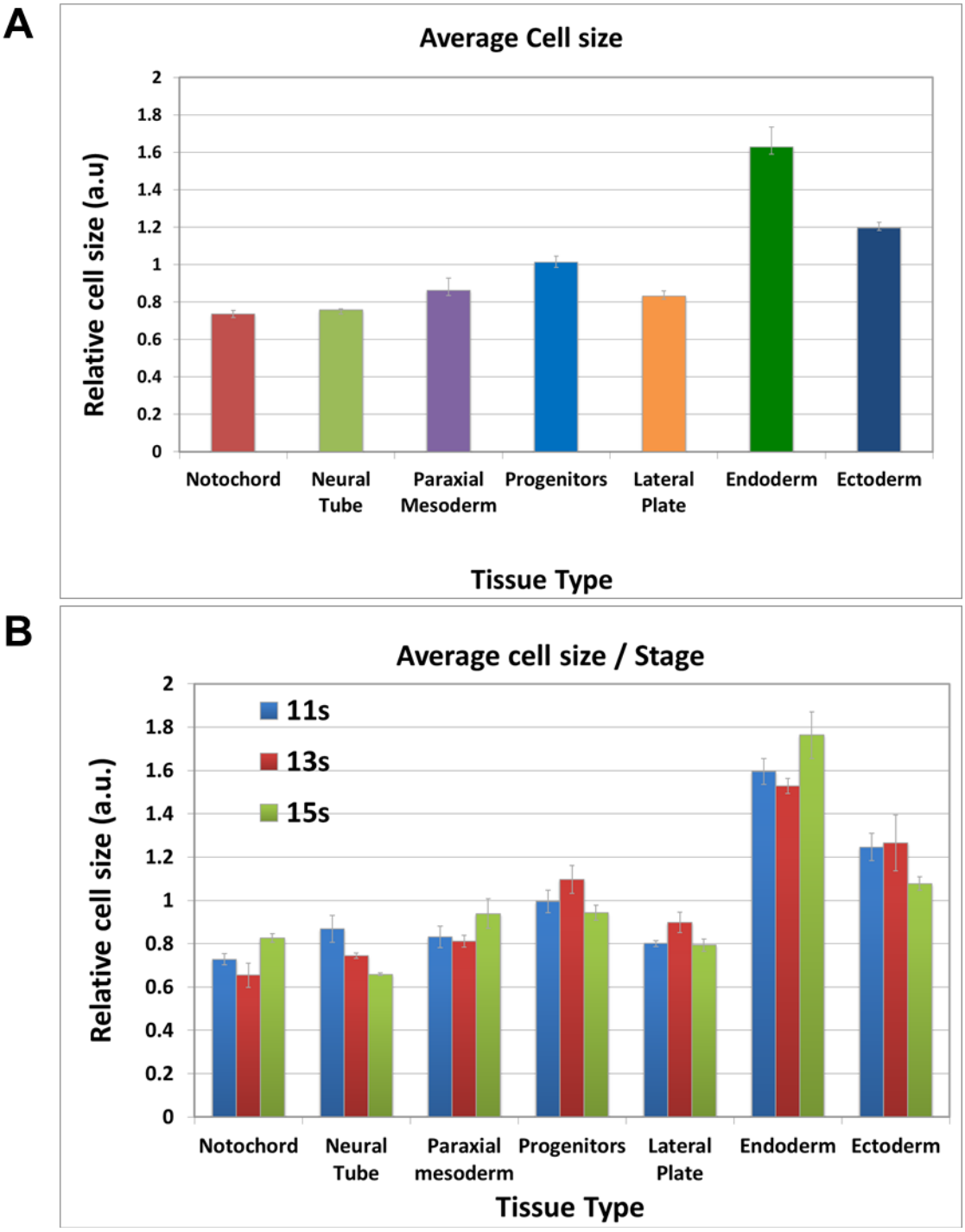

Supplemental Figure 3: Cell size analysis.
A) Comparison between tissues. B) Comparison between stages. Errors bars are SEM; normalized average of more than 30 cells measured in different regions of each tissue from 9 different embryos (3 per stage, see supplementary methods for details).(a.u. stands for arbitrary untis)

A

	neural tube	paraxial	progenitors	lateral mesoderm	endoderm	ectoderm
notochord	0.0002	0.0009	0.0304	0.0004	0.0875	0.0722
neural tube		0.0001	0.0111	0.0239	0.0043	5.4957E-06
paraxial			0.1612	0.3565	0.1539	0.0121
progenitors				0.5432	0.5359	0.0182
lateral mesoderm					0.0692	0.0017
endoderm						0.5488

B

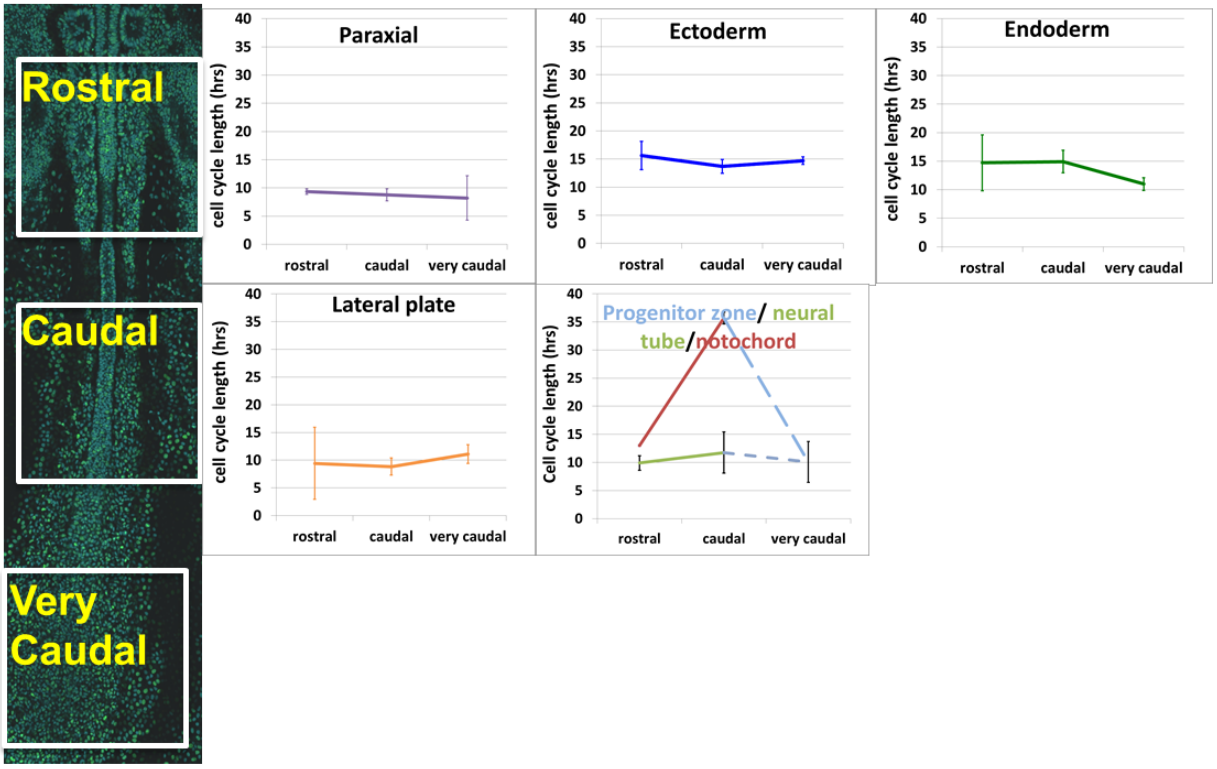

C

	very caudal vs caudal	caudal vs rostral
notochord		0.0027
neural tube		0.5156
paraxial	0.5034	0.4203
progenitors		
lateral mesoderm	0.1145	0.3324
endoderm	0.0945	0.0090
ectoderm	0.5266	0.4456

Supplemental Figure 4: statistical and localized analysis of cell proliferation (associated to Figure 3).

A) Statistical comparison of average cell cycle length values in different tissues by t-test; highlights show conditions in which the differences in densities are statistically different

($p<0.05$) (t-test) n=9. B) Average cell cycle length in different tissues along the anteroposterior axis of the elongating embryo. C) Statistical comparison of average cell cycle length values in A/P locations by t-test; highlights show conditions in which the differences in densities are statistically different ($p<0.05$) n=9.

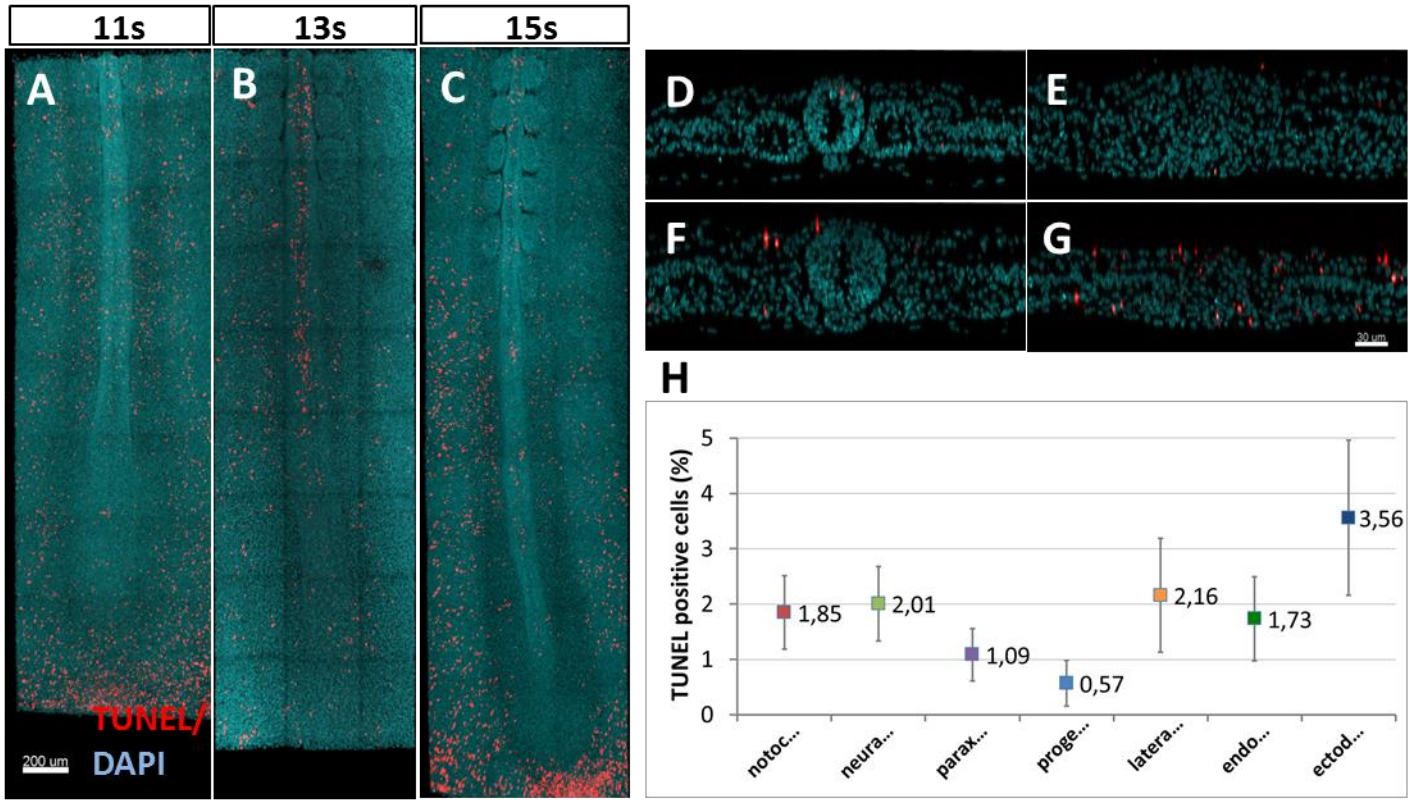

I

	notochord	neural tube	paraxial	lateral mesoderm	progenitors	endoderm	ectoderm
notochord		0.5096	0.6064	0.4577	0.1023	0.3110	0.3164
neural tube			0.8182	0.8182	0.0107	0.4998	0.4579
paraxial				0.4357	0.1977	0.3011	0.3062
lateral mesoderm					0.0254	0.6429	0.4296
progenitors						0.0364	0.1569
endoderm							0.5418
ectoderm							

Supplemental Figure 5: apoptosis analysis during axis extension.
A-C) TUNEL staining (red) and DAPI staining (cyan) at different embryonic stages. 11s (A), 13s (B), 15s (C) (dorsal view, anterior is at the top). D-G) Digital transverse sections of a 13 s stained embryo at different anteroposterior levels (most anterior D, most posterior G). H) Cell death rates (%) were calculated by automatically detecting all nuclei (DAPI channel) and TUNEL positive nuclei in every tissue using the spot function of Imaris. I) Statistical analysis of average cell death rate for different tissues, highlighted areas show conditions in which the differences in densities are statistically different ($p<0.05$, t-test, $n=9$). Errors bars are standard errors of the mean.

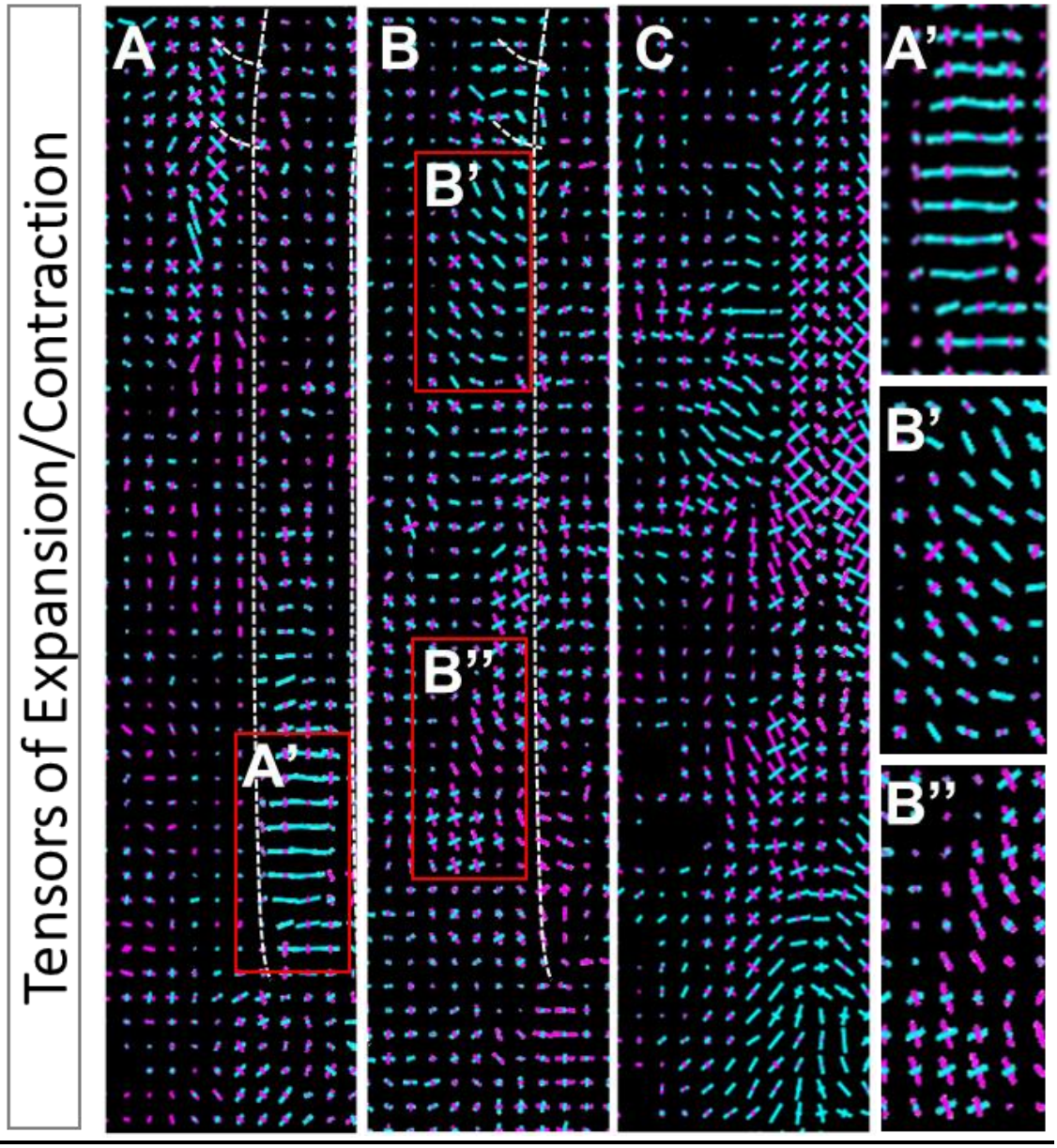

Supplemental Figure 6: Tensor maps without the fluorescent images of the embryo (related to Figure 6 G-I).
(A) represents the most ventral level, (B) intermediate level, (C) the most dorsal level. The compaction values are presented in blue and the expansion values in pink, intensities are represented by length and directionality by their orientation. A', B' and B" are close up views (red rectangles) from A and B. Note the expansion of the caudal ventral region of the embryo has a strong elongation component (A/P axis) (B") whereas the contractions in the anterior part of the PSM (B'), or in the caudal neural tube (A') are mainly due to convergence (mediolateral contraction).

Supplemental movies

Supplemental Movie 1:
H2B-cherry quail embryo filmed from the ventral view with a 10x objective. Note that that tissues seem to elongate toward the posterior pole of the embryo at different velocities, cells in the notochord shown in the red patch move faster than cells in the green patch located in the paraxial mesoderm. Anterior region is on the left.

Supplemental Movie 2:
H2B-cherry quail embryo filmed from the ventral view with a 20x objective. In the first part of the movie all nuclei are shown in white, in the second part of the movie Z stacks have been color coded to see tissue differential movement along the dorsoventral axis. Note that cells from the endoderm (located ventrally, colored coded in red) move toward the posterior direction faster than cells in the PSM (located dorsally compared to the endoderm and color coded in green). Anterior region is on the left.

Supplemental Movie 3:
H2B-cherry quail embryo filmed from the dorsal view with a 10x objective. Note that all tissues seem to elongate toward the posterior pole of the embryo at the same speed, including cells in the neural tube shown in the red patch and ectoderm cells located laterally in a green patch. Anterior region is on the left.

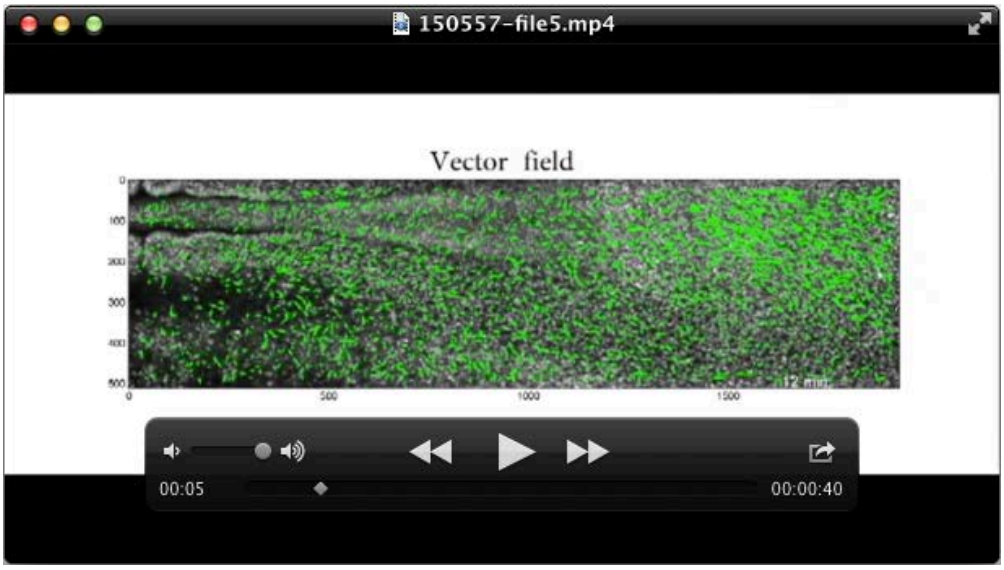

Supplemental Movie 4 (related to figures 5 & 6):
Robustness of vector field and deformation patterns through time. This movie is a series of 3 short movies illustrating the fact that vector field and tissue deformation patterns described in figure 5 and 6 can been seen through different time-points during time-lapse analysis. The time is labeled in white on the bottom right of the movies. Anterior is on the left. H2B-cherry quail embryo filmed from the ventral view with a 20x objective. Z layer selected correspond to the middle of the embryo. Movies of vector field, tissue rotation and expansion are shown as labelled.

Supplementary methods

Volume measurements (related to Supplemental Fig. 1):

Bra and Sox2 3D domains were determined using the Surface function of Imaris. The progenitor region (blue) was delineated using the mask function in order to define the intersection of the Sox2 and Bra volumes. Therefore, this volume corresponds to a region where Sox2 and Bra are highly co-expressed. The caudal PSM (purple) was delineated as the volume containing the low level of Bra, the notochord (red) as a volume containing high level of Bra. The neural tube (green) was delineated as the volume containing the high level of Sox2. The volumes and size measurements (length, width, thickness) of these different surfaces were used to calculate the average values in the graphs.

Density measurement (related to Figure 2):

The K-Nearest Neighbors algorithm can be implemented with a linear search, that is to say that every point is compared against the entire data set. While this approach is the simplest to implement, the runtime of this algorithm is $O(N^2)$, which is unacceptable for large data sets. As an example, using the linear search on a data set of 65,000 points took roughly 16 hours; with the process described below, the same data set ran in two minutes. This naïve implementation of K-Nearest Neighbors can be improved with the inclusion of an appropriate Nearest Neighbor Search**.** For this project the Nearest Neighbor search was implemented in two parts; storing the data with a hierarchical structure, then searching for candidate neighbors within a given search radius. For each data point, a representative element of the lattice as defined in [1] is chosen by proximity. These representatives from the lattice are given Canonical Addresses as described [1]. Lattice points whose Canonical Addresses share a common prefix occupy a contiguous, approximately spherical, region of space; with longer prefixes denoting smaller regions. After every data point is assigned a representative, the data points are lazily inserted into a Prefix Tree, indexed by Canonical Address. As each node of the tree specifies a Canonical Address prefix, the node represents a region of space. Once all data points have been inserted into the prefix tree, data points in a given radius can be found by searching from the root of the tree, which denotes the empty prefix and represents the entire search space, ignoring branches whose corresponding regions of space do not intersect the given radius. If less than K data points are found within the given radius, the radius is increased and the search is carried out again. For each embryo, the different tissues were hand-segmented using Imaris. Next, cellular-position data were extracted using the 'Spots' function of the software, with the diameter of each cell defined as 4.5 μm. The cells were then categorized into tissues based on the hand-segmented regions. Each cell was given an identification number (ID), which is used to link the cell to the tissue wherein it is located. These values were stored in a comma-separated value (csv) file that was inputted into the program detailed **above**.

The output of the k-nearest-neighbors program is a csv file containing the ID of reference cell, its Euclidean vector, followed by the ID of its first nearest neighbor, its Euclidean vector, and its distance (radius) to the reference cell. This continues until a list

is generated for all 'n' neighbors. Through validation testing, it was found that the value of 'n' needed for the most differentiation is 10, or 10 neighbors.

For quantifying the density of each tissue, cells were split into the different tissue types based on their ID number in order to find the global average of all radii for all cells within a specific tissue. This global-average radius was used to find an "average" density for each tissue. Assuming that the volume of interest around each reference cell is a sphere, the equation $V = \frac{4}{3}\pi r^3$ was used with 'r' as the global-average radius per tissue. This value was scaled to 100 μm^3. Since in each region there are 10 cell neighbors, the density was then defined as:

$$density = \frac{Cell\ number\ (10\ cells)}{Volume\ (100\ \mu m^3)}$$

The density map, as seen in **Figure 2**, was constructed using the position of each cell and the average radius to each of its nearest neighbors. Each cell is plotted in 3D- space and colored to represent its density type. The density was calculated as seen above, however, instead of a global average; the radius is defined as the average radius of the 10 nearest neighbors of each cell. Cells that are in a low density region (blue cells) represented average-densities of less than 1,382 cells per 100 μm^3; those that are in high density regions (red cells) represented average-densities greater than 2,388 cells per 100 umm^3 ; and those that are in medium-density regions (yellow cells) represent average-densities that fall in between the two ranges. Slices were then made in each region to further show variations within tissues.

Cell size estimation analysis (related to Supplemental Figure 3):

Fixed quail embryos at different stages stained with nucleus (Nucblue, Thermofisher) and actin (Actingreen 488 ready probes Thermofisher) staining have been imaged at the confocal imaging. Cell size by tissue has been evaluated using Imaris software by measuring length (L) and width (W) of cells using the phalloidin staining to estimate the cell boundaries. An example of a measurement is shown in the image below for a cell in the endoderm. An estimated cell area as a proxy of cell size has been calculated by multiplying those values for each cell. Estimated cell sizes have been filtered for aberrant measurement and normalized by embryo.

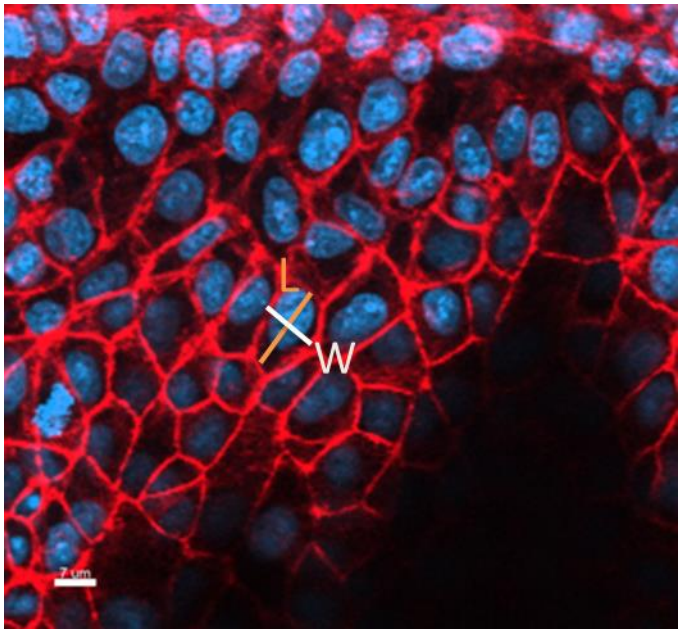

Cell cycle duration calculation (related to Figure 3 and supplemental Figure 4):

For each tissue the different EdU incorporation rates >30% and <100% were plotted in function of the length of the pulses. We assume that all cells in this part of the embryo are in the cell cycle. A linear regression was fitted to these different incorporation rates and the slope of this linear regression was used to calculate the cell cycle length for each tissue : cell cycle time = 100 / slope of the linear regression (Nowakowski et al. 1989) as illustrated below:

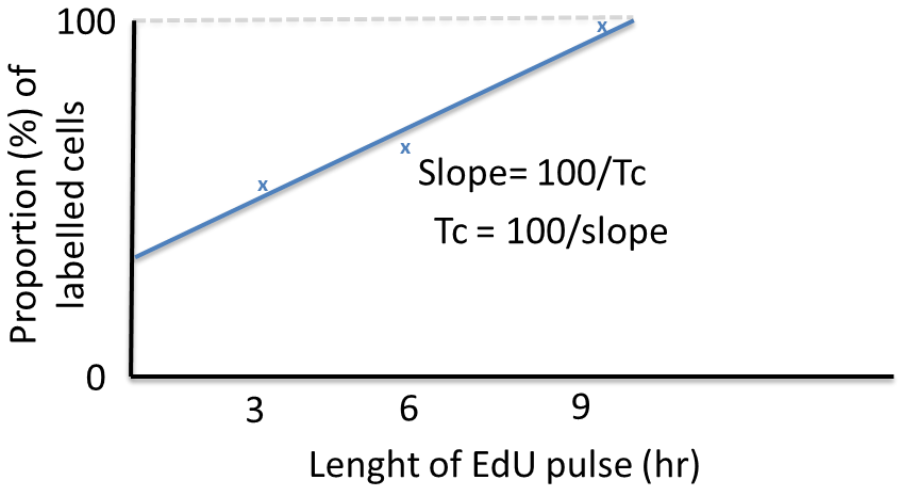

Fitting of tissue proliferation variables to tissue elongation (related to Figure 4):

Stage 11s posterior tissue lengths were measured from the 10th somite to caudal limit of the tissue at as described in Fig 1. These lengths were multiplied by the doubling time (measures shown in Fig. 3) of each tissue in a hypothetical situation of 6 h of A/P elongation only due to proliferation (see schema below for example). Simulated tissue lengths at 15s (sL15s) were obtained by multiplying the average tissue lengths at 11s (L11s) with each specific cell cycle times (CCT) (Figure 3) for 6h: sL15s=L11s + (6/CCT) *L11s. The tissue lengths measured at 15s (Fig 1) were then compared to the simulated 15s tissue lengths.

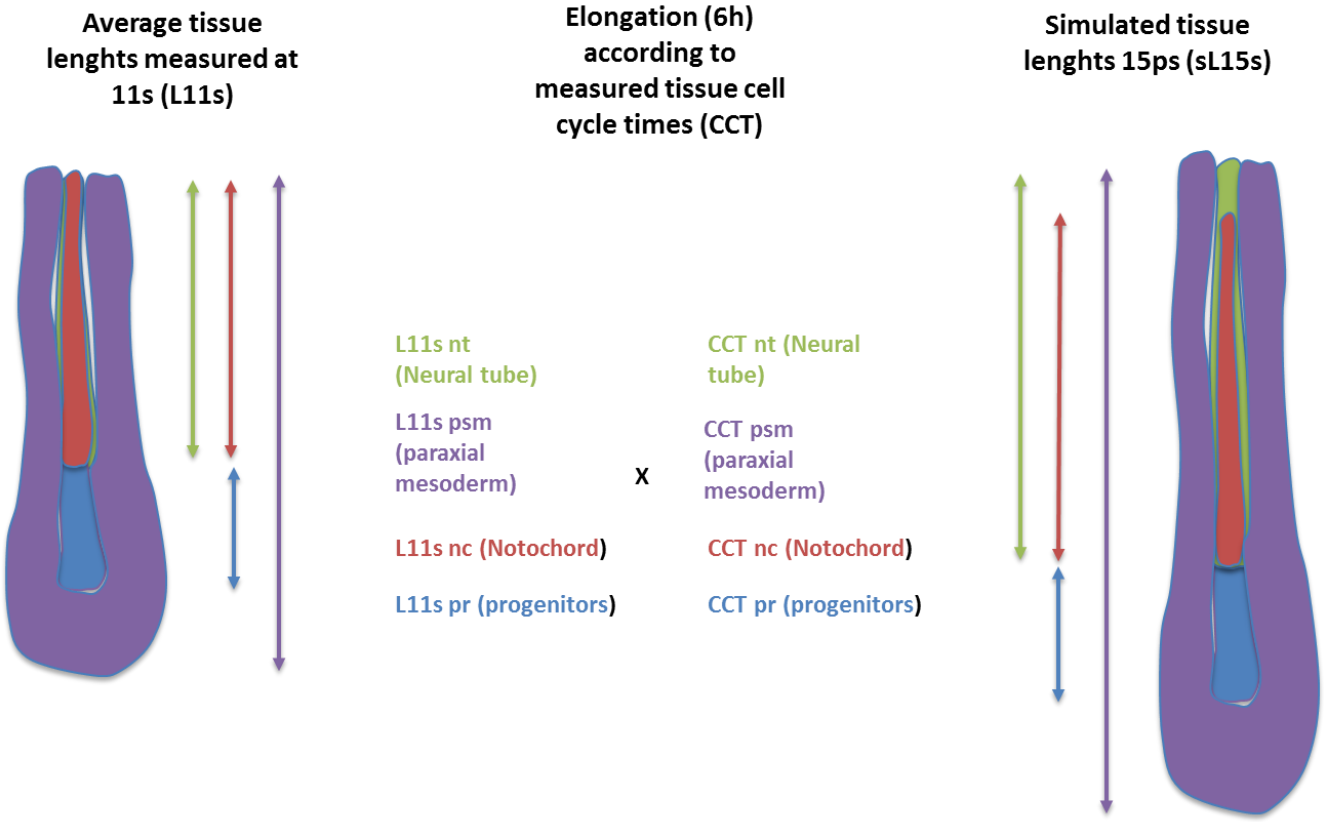

Cellular tracking algorithm (related to Figure 5 and 6):

Cellular tracking is built on three steps:

- Cellular detection
- Cross-correlation between successive time frames
- Correction of cellular displacement using a matching algorithm

Cellular detection:

In order to detect cells, the choice that was made is to look for local maxima of intensity that are defined as pixels whose value is higher than any of their eight neighbors. Indeed, cells in the embryo have various shapes and are not always well defined visually (endoderm cells are big and have clear contours whereas cells in the posterior axial mesoderm are not so easily distinguished) so that it is very difficult to do a cellular segmentation based on a predefined shape. On the other hand, detecting maxima is an easy and efficient procedure, which does not assume a lot on the geometry of cells (an estimate of their typical size is the only parameter that is needed). Additionally, subsequent analysis for motion detection relies on cross-correlation, which takes advantage of this diversity in shape to provide an estimation of the displacement. Detection of local maxima of intensity is also a generic procedure that is easily adapted to different data (i.e. different embryos).
To detect local maxima of intensity, data is convoluted with a Gaussian filter to eliminate short-range details. Local maxima of the image are then easily detected. Only those whose intensity is higher than a given threshold are kept, the rest is considered as lying in the background of the image. This threshold is computed using the so-called Otsu's method [2], which is a convenient way to separate pixels in an image between background and foreground.

Cross-correlation:

The previous method gives a list of cell's positions whose displacement is then measured using cross-correlation. It relies on the computation of a quantity Cor(u,v) that depends on a presumptive displacement (u,v) of the cell. Figure 1 illustrates how Cor(u,v) is computed.

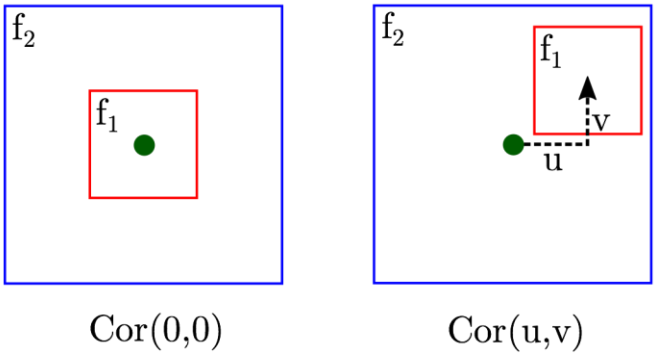

Figure 1: Cross correlation method.
A sample of the first image (f_1) is isolated, as well as a larger sample of the second image (f_2). Sample f_1 is then displaced over all possible positions (u,v) in f_2 and the cross correlation is then calculated.

The cross-correlation Cor(u,v) is defined as:

$$\mathrm{Cor}(u,v) = \frac{\sum_{a,b}(f_1(a,b) - < f_1 >)(f_2(a+u,b+v) - < f_2 > (u,v))}{(\sum_{a,b}(f_1(a,b) - < f_1 >)^2)^{1/2}(\sum_{a,b}(f_2(a+u,b+v) - < f_2 > (u,v))^2)^{1/2}}$$

Where the $<f_1>$ is the average of f_1 and $<f_2(u,v)>$ is the average of f_2 in the region spanned by f_1 at position (u,v) (i.e. the average of f_2 in the red square on Figure 1). The sums on the expression above run over all positions in image f_1.
Intuitively, Cor(u,v) quantifies how much f_1 and f_2 look like it each other at position (u,v). The higher Cor(u,v), the higher f_1 and f_2 look similar for the corresponding displacement. Cellular motion is then estimated as the displacement (u,v) that maximizes Cor(u,v).

-Matching.

Cross-correlation produces a displacement vector (u,v) for every cell detected at step 1. However, this displacement does not in general match the cell of the first frame to a cell detected in the second frame. Therefore, the last step is a matching procedure that ensures that displacements calculated are proper cell matching. This part of the tracking algorithm is inspired by [3] and consists of doing the minimal modification of cellular displacements that produces a consistent matching between cells.

Local averages and regularization:

The tracking algorithm produces a set of cell positions and displacements at every time and depth in the embryo. Tissue analysis presented in the paper requires a change of scale, i.e. instead of considering each individual displacement, we are interested in local average of these quantities. To achieve this averaging, displacement vectors located at cell positions are replaced by averages on a regular 2D grid.

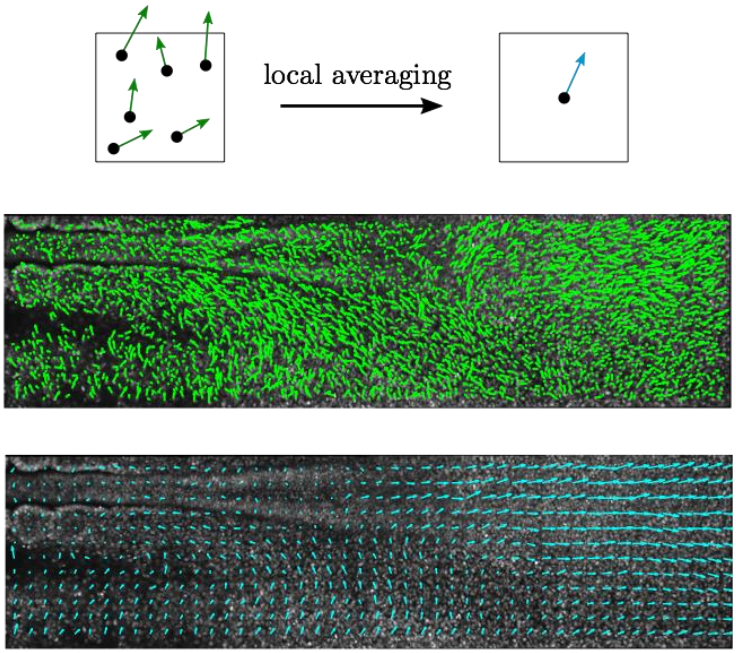

Figure 2: Local averages of cell displacements. Following the scheme described on the first row, displacement vectors (second row) positioned at cell positions are replaced by their local average on a regular grid (third row).

Quantities computed and presented in the main text are used to characterize local expansion and rotation in the tissues. Those quantities are related to the spatial derivative of the velocity field (or equivalently of the displacement field). For data similar to that presented on Figure 2 (last row), those spatial derivatives are easily computed by a finite difference scheme. For example:

$$\frac{\partial v_{x,i,j}}{\partial x} \approx \frac{v_{x,i+1,j} - v_{x,i-1,j}}{2\Delta x}$$

Where (i,j) is the position of the grid (i is the x-axis index and j the y-axis index), v_x is the x component of the velocity and Δx is the distance on the x-axis between two neighboring points of the grid. Unfortunately, averaged data is too noisy for such computation: neighboring displacement vectors on the grid are sometimes too different for the approximation of the first derivative by finite difference to hold. To circumvent this issue, an additional regularization method is used. This method is inspired by machine learning methods and rely on the assumption that cells in a given square of the grid, at position (i,j) have a velocity that is the sum of a velocity $\mathbf{v}_{i,j}$ and a Gaussian noise of zero mean and variance σ^2. As a consequence, the empirical average of the cells' velocities in a square at position (i,j), $\mathbf{c}_{i,j}$, is modeled as the sum of $\mathbf{v}_{i,j}$ and a Gaussian noise of zero mean and variance $\sigma^2/N_{i,j}$ where $N_{i,j}$ is the number of cells detected in square at position (i,j).The goal

of the regularization is to infer the value of the unknown velocity field $\{\mathbf{v}_{i,j}\}$ with a constraint on the smoothness of the field (so that finite difference approximation of spatial derivatives is possible). Bayesian inference leads to the minimization to the following function for the estimation of $\{\mathbf{v}_{i,j}\}$

$$J_\lambda(\{\mathbf{v}_{i,j}\}) = \sum_{\substack{i,j \\ N_{i,j}\neq 0}} N_{i,j}(\mathbf{c}_{i,j} - \mathbf{v}_{i,j})^2 + \lambda \sum_{i,j} \sum_{(k,l)\in\mathcal{N}_{i,j}} (\mathbf{v}_{k,l} - \mathbf{v}_{i,j})^2$$

The two terms in the definition of this cost have different meaning:

- The minimization of the first term ensures that the final velocity field $\{\mathbf{v}_{i,j}\}$ is not too far from the data $\{\mathbf{c}_{i,j}\}$. The sum of the square distance between $\mathbf{v}_{i,j}$ and $\mathbf{c}_{i,j}$ is weighted by the number of cells in each square of the grid, so that more emphasis is given to regions in the embryo were a lot of data is available.
- The second term is a regularization term. It has a big value if neighboring points on the grid have velocities $\mathbf{v}$ that are too far from each other.

The combination of those two terms in the cost function J_λ depends on a parameter λ that quantifies the relative importance of the regularization term. A high value for λ means that more importance is given to the regularization term, meaning that finite difference scheme is more and more valid. On the other hand, the final velocity field is more and more different from the data as λ increases. A suitable value for λ is found by setting:

$$r(\lambda) = \frac{\displaystyle\sum_{\substack{i,j \\ N_{i,j}\neq 0}} N_{i,j}(\mathbf{c}_{i,j} - \mathbf{v}_{i,j})^2}{\displaystyle\sum_{\substack{i,j \\ N_{i,j}\neq 0}} \sigma_{i,j}^2} = 1$$

where for each position (i,j), $\sigma^2_{i,j}$ is the estimation of the sum of the variance of the x and y components of the velocities detected in the square (i,j). Intuitively, setting $r(\lambda)$ to 1 means that the $\{\mathbf{v}_{i,j}\}$ can deviate from the $\{\mathbf{c}_{i,j}\}$ as much as what the noise of the data allows. Theoretically, λ has to be computed for each specific piece of data. Practically though, λ was set once and for all by calculating its value for each time frame and depth (using the criterion $r(\lambda)=1$) and choosing the minimum. Indeed, since lower λ means that $\{\mathbf{v}_{i,j}\}$ is closer to $\{\mathbf{c}_{i,j}\}$ than the maximum allowed deviation, this approach is legitimate.

Finally, quantities characterizing tissue kinematics can be extracting using finite difference schemes described above. They rely on the estimation of spatial derivatives, which is done as follows

$$\frac{\partial v_{x,i,j}}{\partial x} \approx \frac{v_{x,i+1,j} - v_{x,i-1,j}}{2\Delta x}$$
$$\frac{\partial v_{x,i,j}}{\partial y} \approx \frac{v_{x,i,j+1} - v_{x,i,j-1}}{2\Delta y}$$
$$\frac{\partial v_{y,i,j}}{\partial x} \approx \frac{v_{y,i+1,j} - v_{y,i-1,j}}{2\Delta x}$$
$$\frac{\partial v_{y,i,j}}{\partial y} \approx \frac{v_{y,i,j+1} - v_{x,i,j-1}}{2\Delta y}$$

Where Δx and Δy are the grid spacing in the x and y direction respectively. They are chosen equal in our analysis.

The quantities computed and displayed in the main text are:

- The divergence $$\frac{\partial v_x}{\partial x} + \frac{\partial v_y}{\partial y}$$

- The curl $$\frac{\partial v_y}{\partial x} - \frac{\partial v_x}{\partial y}$$

- The strain tensor d, which is a 2D matrix

$$d = \frac{\nabla \mathbf{v}^T + \nabla \mathbf{v}}{2}$$

with

$$\nabla \mathbf{v} = \begin{pmatrix} \frac{\partial v_x}{\partial x} & \frac{\partial v_x}{\partial y} \\ \frac{\partial v_y}{\partial x} & \frac{\partial v_y}{\partial y} \end{pmatrix}$$

Diagonalization of d gives the eigenvectors and eigenvalues showed in the main text.

Biliography

[1] Kitto W. An isomorphism between the p-adic integers and a ring associated with a tiling of N-space by permutohedra.
Discrete Applied Mathematics archive
Volume 52 Issue 1, July 22, 1994
[2] N Otsu. A Threshold Selection Method from Gray-Level Histograms. IEEE Transactions on Systems, Man, and Cybernetics, 9(1):62–66, 1979.
[3] I. F. Sbalzarini and P. Koumoutsakos. Feature point tracking and trajectory analysis for video imaging in cell biology. Journal of Structural Biology, 15